ADVANCED FUNCTIONAL MATERIALS
www.afm-journal.de

A Bone-Targeting Hydrogen Sulfide Delivery System for Treatment of Osteoporotic Fracture via Macrophage Reprogramming and Osteoblast-Osteoclast Coupling

Yi Qin, Zhen Zhang, Xiaobin Guo, Wenhao Li, Wenyu Xia, Gaoran Ge, Yanyue Li, Min Guan, Ang Gao, Lu Mao,* Huaiyu Wang,* Paul K. Chu, and Dechun Geng**

The demand for systemic treatment of osteoporotic fractures to reduce recurrence is increasing, but current anti-osteoporosis medications exhibit unsatisfactory efficacy due to adverse events and limited effects on fracture healing. Herein, a bone-targeting zeolitic imidazolate framework-8 (ZIF)-based hydrogen sulfide (H_2S) delivery system (ZIF-H_2S-SDSSD) is designed to simultaneously promote fracture healing and alleviate osteoporosis. With bone-targeting peptide SDSSD grafted on the surface, ZIF-H_2S-SDSSD nanoparticles release H_2S in bone tissues without affecting the serum H_2S level, thereby mitigating potential risks of systematic H_2S delivery. Upon cellular uptake, the acidic environment in lysosomes drives the release of H_2S from the encapsulated zinc sulfide in conjunction with the degradation of ZIF. The synergistic effects of released Zn^{2+} and H_2S promote macrophage metabolic reprogramming by suppressing succinate accumulation and mitochondrial reactive oxygen species (mtROS) production, and further regulate osteoblast-osteoclast coupling. Overall, this strategy holds great promise in the clinical treatment of osteoporotic fractures and broadens the application of nanomedicine therapy for orthopedic diseases.

1. Introduction

Osteoporotic fracture is a serious consequence of osteoporosis, which is characterized by reduced bone mass and deterioration of bone microarchitecture.[1] The incidence of osteoporotic fracture continues to rise in aging society, posing a significant challenge in both treatment and prevention.[2] The prolonged healing period, resulting from compromised bone regeneration, leads to higher recurrence and disablement rates, particularly in elderly patients.[3] Although surgery is the primary treatment for bone fractures, it fails to prevent further bone loss, so systemic treatments are necessary to reduce recurrent osteoporotic fractures and promote long-term survival.[4] Current anti-osteoporosis medications, such as bisphosphonates, denosumab, raloxifene, strontium ranelate, and teriparatide, have been shown to prevent the recurrence of osteoporotic fractures.[5] However, these medications lack targeted delivery, thus resulting in increased adverse events and unsatisfactory outcomes.[6] Furthermore, most of these medications function via a single mechanism, and their therapeutic effects on fracture healing are limited.[7] Therefore, it is highly desirable to develop therapies that simultaneously promote fracture healing and alleviate osteoporosis.

Y. Qin, W. Li, W. Xia, G. Ge, D. Geng
Department of Orthopedics
The First Affiliated Hospital of Soochow University
Orthopedic Institute
Medical College
Soochow University
Suzhou, Jiangsu 215006, China
E-mail: szgengdc@suda.edu.cn

Z. Zhang, Y. Li, M. Guan, A. Gao, H. Wang
Center for Human Tissues and Organs Degeneration
Shenzhen Institute of Advanced Technology
Chinese Academy of Sciences
Shenzhen 518055, China
E-mail: ang.gao1@siat.ac.cn; hy.wang1@siat.ac.cn

The ORCID identification number(s) for the author(s) of this article can be found under https://doi.org/10.1002/adfm.202418822

DOI: 10.1002/adfm.202418822

X. Guo
Department of Orthopedics
First Affiliated Hospital of Xinjiang Medical University
Urumqi, Xinjiang 830054, China

L. Mao
Department of Spine Surgery
Zhongda Hospital
Southeast University
Nanjing, Jiangsu 210009, China
E-mail: 101012005@seu.edu.cn

H. Wang
The Key Laboratory of Biomedical Imaging Science and System
Chinese Academy of Sciences
Shenzhen 518055, China

P. K. Chu
Department of Physics
Department of Materials Science and Engineering, and Department of Biomedical Engineering
City University of Hong Kong
Tat Chee Avenue, Kowloon, Hong Kong 999077, China

Fracture healing requires a suitable microenvironment conducive to osteoclast-osteoblast coupling. The host immune response is intimately involved in this process, especially during the early inflammatory healing phase.[8] Neutrophils migrate to the fracture site first and are replaced by monocytes within 24 to 48 h, which then differentiate into macrophages.[9] Macrophages act as the coordinators of the fracture healing process because they secrete multiple cytokines to regulate the microenvironment. Generally, macrophages are classified into two primary subtypes: inflammatory M1 macrophages and anti-inflammatory M2 macrophages. Although M1 macrophages are essential to the initiation of the healing process, prolonged and excessive M1 polarization inhibits fracture healing, highlighting the importance of a timely transition from M1 to M2 phenotype.[10] Metabolic reprogramming plays a predominant role in regulation of macrophage phenotypes. M1 macrophages exhibit enhanced glycolytic metabolism and inhibited mitochondrial oxidative phosphorylation (OXPHOS), while M2 macrophages are characterized by an intact tricarboxylic acid (TCA) cycle and upregulated OXPHOS. The crosstalk between the metabolic pathways and cellular signaling can dramatically induce specific immune functions, rather than simply affecting energy production or general biosynthesis.[11] Since macrophages in vivo are exposed to an extended range of stimuli and do not fully fit into the binary M1/M2 frame, focusing on the metabolic characteristics of different macrophage subsets will broaden our understanding of their specific phenotypes, which is critical to the development of therapeutics based on macrophage regulation.[12]

Besides nitric oxide (NO) and carbon monoxide (CO), hydrogen sulfide (H_2S) has been identified as the third endogenous gasotransmitter.[13] A reduced serum H_2S level has been reported in the ovariectomy (OVX)-induced osteoporosis mouse model and exogenous H_2S treatment is considered a novel therapeutic approach.[14] H_2S exerts extensive effects on various cell components in the bone tissue microenvironment, such as facilitating osteogenic differentiation, inhibiting osteoclastic differentiation, and regulating macrophage polarization. These therapeutic effects of H_2S are largely attributed to its antioxidant capacity, which protects cells from excessive reactive oxygen species (ROS).[15] Despite its therapeutic potential, the clinical application of H_2S is challenging due to its narrow therapeutical window. Commonly used H_2S donors often exhibit uncontrolled H_2S release, leading to potential toxic effects even at low doses. Furthermore, most of the current exogenous H_2S treatments inevitably increase the serum H_2S level and raise safety concerns.[16] As osteoporosis is a systemic metabolic bone disease, a targeted delivery strategy is essential for H_2S-based therapeutics in treating osteoporotic fractures.

Zeolitic imidazolate framework-8 (ZIF), a subclass of metal-organic frameworks (MOFs) composed of metal ions and organic linkers, is widely used as a drug delivery platform due to its easy fabrication, low cytotoxicity, and high drug loading efficiency.[17] Particularly, nanoscale ZIF is stable under physiologically neutral conditions and decomposes in acidic environments, such as tumor microenvironment and acidic organelles, making it suitable for pH-responsive delivery. Basically, ZIF is constructed from Zn^{2+} and 2-methylimidazole (2-MIM) via coordination. As an essential trace element, zinc plays crucial roles in various biological processes, including immunoregulation and osteogenic differentiation.[18] Additionally, Zn^{2+} exhibits a high affinity to thiol and sulfide groups and protects them from oxidation. This interaction is involved in numerous biochemical processes, such as the structural stabilization of metalloproteins and the catalytic activity of zinc enzymes.[19]

Herein, a bone-targeting H_2S delivery system is designed by encapsulating acid-labile zinc sulfide into ZIF (ZIF-H_2S) and further modification of the surface of ZIF-H_2S nanoparticles (NPs) with a bone-targeting peptide Ser-Asp-Ser-Ser-Asp (SDSSD). As illustrated in **Scheme 1**, before mixing with 2-MIM to form ZIF, a portion of Zn^{2+} is chelated by HS^- to form zinc sulfide. The ZIF-H_2S NPs encapsulating zinc sulfide are then surface-modified with SDSSD, which is coupled with cysteine to facilitate the coordination bonds between thiol groups and zinc ions on the ZIF surface. The ZIF-H_2S-SDSSD NPs can target bone tissues after intravenous administration in osteoporotic fracture mice. Upon cellular uptake, the acidic environment in lysosomes drives the release of H_2S from the acid-labile zinc sulfide along with the degradation of ZIF. The synergistic effects of released Zn^{2+} and H_2S promote macrophage metabolic reprogramming by suppressing succinate accumulation and mitochondrial reactive oxygen species (mtROS) production, and further regulating osteoblast-osteoclast coupling. This ZIF-based H_2S delivery system with bone-targeting capability holds great promise in treating osteoporotic fractures.

2. Results and Discussion

2.1. The Imbalance of Macrophage Polarization is Associated with Impaired Fracture Healing in Osteoporotic Mice

To assess the impact of osteoporosis on fracture healing, osteoporosis is induced in 8-week-old mice by ovariectomy (OVX), followed by femur fracture induction four weeks later. The mice are sacrificed on the 7th, 14th, and 28th day after surgery to evaluate fracture healing. Micro-computed tomography (micro-CT) of the trabeculae under the distal femur growth plate reveals that the OVX group has smaller bone volume/tissue volume (BV/TV), bone surface/tissue volume (BS/TV), trabecular number (Tb.N), and higher trabecular separation (Tb.Sp) compared with the sham group (Figure S1A–F, Supporting Information). Furthermore, the callus BV/TV in the OVX group is consistently lower than that of the sham group at different time points, suggesting impaired fracture healing in osteoporotic mice (Figure S1G, Supporting Information). Given the crucial role of macrophages in fracture healing process, the macrophage phenotypes on the 7th day after surgery are evaluated by immunofluorescence staining. Macrophages in callus are determined by F4/80 labeling, while the transition from M1 to M2 phenotype is identified by CD86 and CD206. Compared with the sham group, OVX group exhibits more F4/80$^+$/CD86$^+$ cells and fewer F4/80$^+$/CD206$^+$ cells, indicating the imbalance of macrophage polarization in osteoporotic fracture callus (Figure S2, Supporting Information). The inflammatory immune microenvironment can be attributed to the reduced estrogen level in OVX-induced mice, resulting in an impaired healing process.[20] Hence, immune dysregulation emerges as a potential target for promoting osteoporotic fracture healing under osteoporotic conditions.

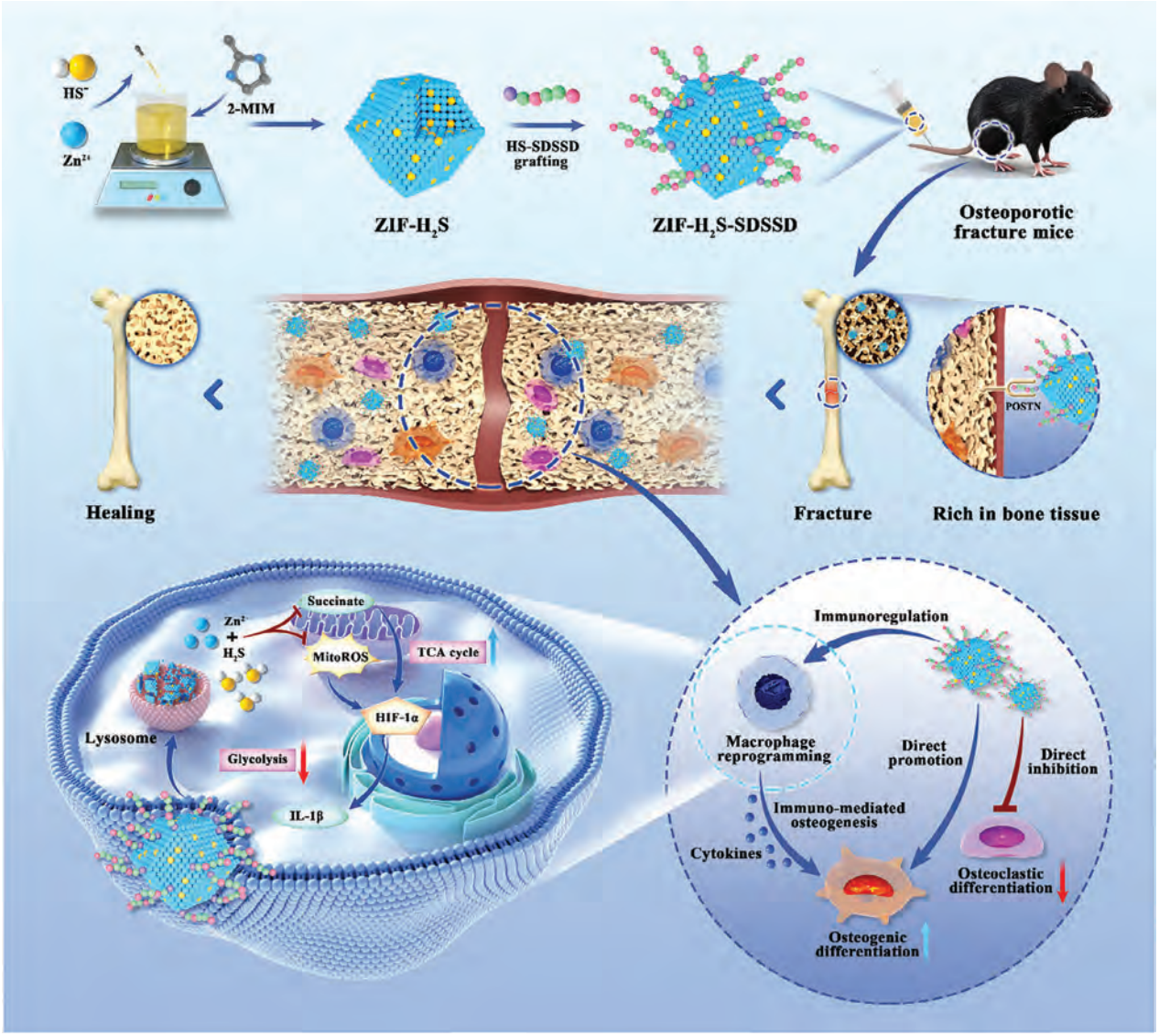

Scheme 1. Schematic illustration of the preparation and therapeutic mechanism of ZIF-H_2S-SDSSD NPs for treatment of osteoporotic fracture.

2.2. Synthesis and Characterization of ZIF-H_2S-SDSSD NPs

The ZIF NPs are prepared using an established procedure by mixing Zn^{2+} with 2-MIM in solution. In the synthesis of ZIF-H_2S NPs, NaHS is added to the Zn^{2+} solution prior to the addition of 2-MIM. Subsequently, the bone-targeting peptide SDSSD is grafted onto the surface of ZIF and ZIF-H_2S NPs by utilizing the coordination bonds between thiol groups and Zn^{2+}. This is accomplished by simply resuspending ZIF and ZIF-H_2S NPs in the SDSSD peptide solution and stirring for 30 min. After centrifugation, the concentration of SDSSD peptides in the supernatant decreases significantly, indicating the successful binding of SDSSD peptides onto the NPs (Figure S3A, Supporting Information). The samples are denoted as ZIF-SDSSD and ZIF-H_2S-SDSSD, respectively.

Scanning electron microscopy (SEM) and transmission electron microscopy (TEM) show that all the fabricated NPs have dodecahedral morphology with a particle size of ≈150 nm (**Figure** 1A). Elemental mapping by energy-dispersive X-ray spectroscopy (EDS) discloses uniform distributions of N, O, Zn, and S in the ZIF-H_2S-SDSSD NPs, with the highest S concentration observed from ZIF-H_2S-SDSSD NPs (Figure 1B; Figure S4; Table S1, Supporting Information). X-ray diffraction (XRD) confirms that the synthesized ZIF NPs closely match the simulated pattern. The other three groups of NPs retain the characteristic peaks of ZIF NPs (Figure 1C), indicating that zinc sulfide doping and surface grafting of SDSSD peptide have little influence on the crystal structure of ZIF NPs. The high-resolution X-ray photoelectron spectroscopy (XPS) spectra only show the S 2*p* peaks from ZIF-SDSSD and ZIF-H_2S-SDSSD groups, confirming successful surface grafting of SDSSD peptides (Figure 1D; Figure S5, Supporting Information). According to the Brunauer-Emmett-Teller (BET) results, the specific surface areas of ZIF and ZIF-H_2S NPs decrease slightly after grafting with SDSSD

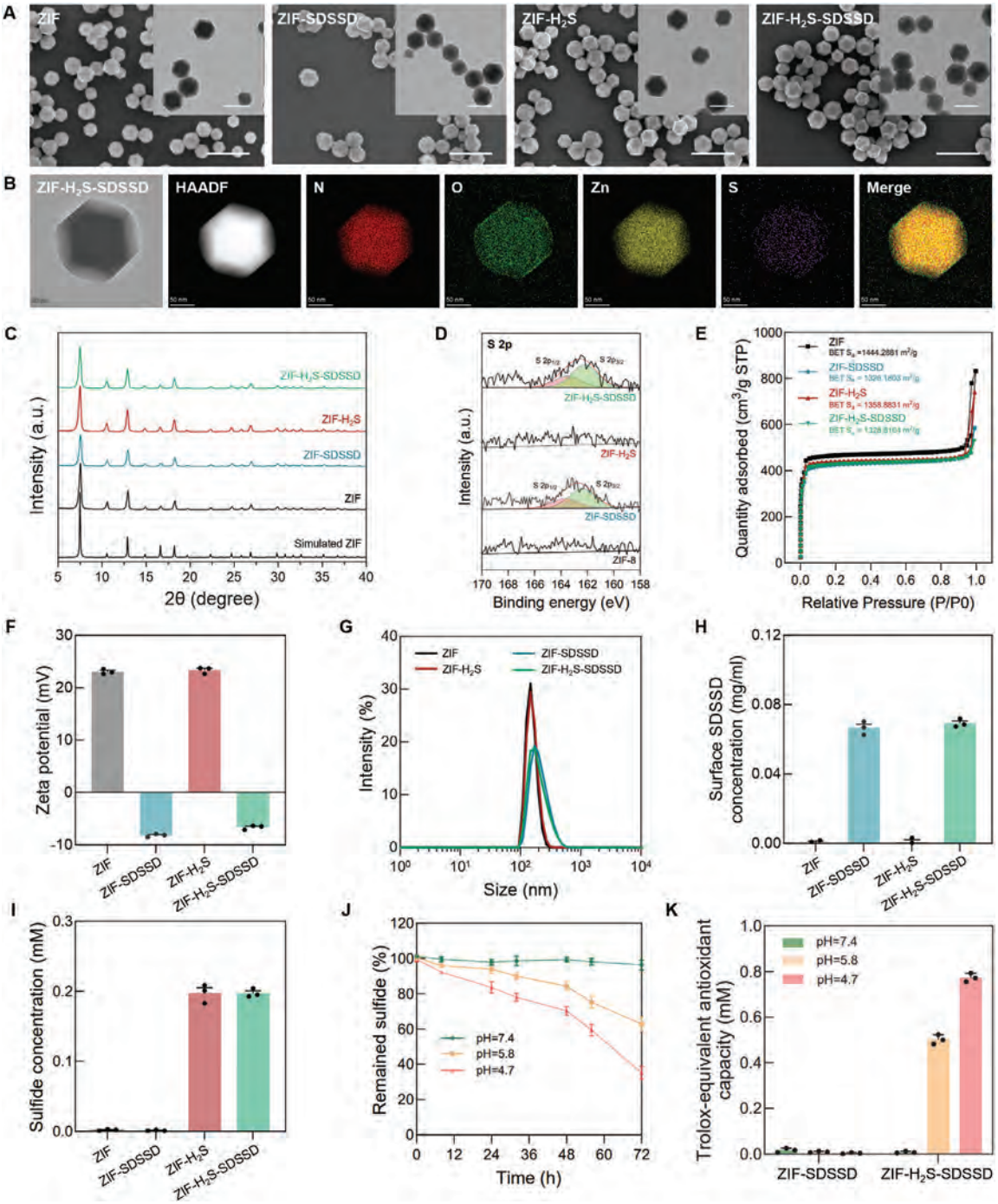

Figure 1. Characterizations of different NPs. A) SEM and TEM images of different NPs (SEM: scale bar = 500 nm, TEM: scale bar = 200 nm). B) Elemental mapping of ZIF-H_2S-SDSSD NPs (scale bar = 50 nm). C) XRD, D) High-resolution XPS S 2*p* spectra, E) BET, F) Zeta potential examination, and G) DLS of different NPs. H) Nominal concentrations of SDSSD peptides grafted onto the outer surface of different NPs ($n = 3$ per group). I) MB assay of different NPs ($n = 3$ per group). J) Remained sulfide in ZIF-H_2S-SDSSD NPs after incubation under different pH conditions for up to 72 h ($n = 3$ per group). K) Trolox-equivalent antioxidant capacity of ZIF-SDSSD NPs and ZIF-H_2S-SDSSD NPs under different pH conditions ($n = 3$ per group).

peptides (Figure 1E; Table S2, Supporting Information). The zeta potentials indicate that the particle surface charge changes from positive to negative after SDSSD grafting (Figure 1F). Dynamic light scattering (DLS) indicates that the particle size of ZIF and ZIF-H_2S is similar, but that of ZIF-SDSSD and ZIF-H_2S-SDSSD is a little larger (Figure 1G; Table S3, Supporting Information). The presence of SDSSD peptides on ZIF-SDSSD and ZIF-H_2S-SDSSD NPs is confirmed by the BCA protein assay. The nominal concentrations of SDSSD peptides grafted on the outer surface of the NPs are determined by direct reaction with the working

reagents (Figure 1H), while those loaded into NPs are assessed after dissolution in an acidic solution (Figure S3B, Supporting Information). The similar results obtained by both methods indicate that almost all the added SDSSD peptides are grafted onto the surface of NPs.

Endogenously generated H_2S has emerged as a pivotal gasotransmitter in various physiological events. Notably, H_2S exhibits a particular affinity to biologically relevant metal ions such as Cu^{2+}, Fe^{2+}, and Zn^{2+}, which usually serve as the central metal catalytic sites in metalloenzymes.[21] Inspired by this peculiarity, we load the acid-labile zinc sulfide within ZIF NPs for H_2S delivery. During the formation of ZIF NPs, the common H_2S donor NaHS is added to the Zn^{2+} solution. A portion of Zn^{2+} is chelated by HS^- stemming from the hydrolysis of NaHS, and subsequently encapsulated into the ZIF NPs. The presence of zinc sulfide in ZIF-H_2S and ZIF-H_2S-SDSSD NPs is confirmed by methylene blue (MB) assay (Figure 1I). Under acidic conditions, ZIF NPs degrade gradually, and H^+ ions also drive acid-labile zinc sulfide into the gas phase to release H_2S. As shown in Figure 1J, the total sulfide content of ZIF-H_2S-SDSSD NPs remains constant in the phosphate buffer solution (PBS) at a pH of 7.4 (simulating the normal physiological condition). In contrast, the sulfide content decreases gradually with time at a pH of 5.8 (simulating the pathological condition) and diminishes further at a more acidic pH of 4.7 (simulating the endo-lysosomal environment). Similarly, the time-dependent release profiles of Zn^{2+} from NPs in PBS solutions with different pH values demonstrate a pH-responsive effect. The release of Zn^{2+} from all NPs is notably slow at pH = 7.4, while both the release rate and cumulative amount of Zn^{2+} increase significantly at pH = 5.8, with even more pronounced increases observed at pH = 4.7 (Figure S6, Supporting Information). The antioxidant capacity of ZIF-SDSSD and ZIF-H_2S-SDSSD NPs also is examined under different pH conditions. As shown in Figure 1K, the ZIF-SDSSD NPs provide little antioxidant effects at different pH values. In contrast, the antioxidant ability of ZIF-H_2S-SDSSD NPs displays a pH-dependent trend in line with that of H_2S and Zn^{2+} release. The pH-dependent behavior bodes well for the targeted therapeutic application of ZIF-H_2S-SDSSD NPs, as the NPs remain stable during systemic circulation and release H_2S upon cellular uptake (into the endo-lysosomes) at bone tissues.

2.3. Biocompatibility and Intracellular Delivery

The cytocompatibility of various NPs is evaluated using the cell counting kit-8 (CCK-8) assay after culturing with bone marrow macrophages (BMMs) and bone marrow-derived mesenchymal stem cells (BMSCs) for 24 h and 72 h. The isolated BMSCs are identified using flow cytometry, exhibiting a phenotype of $CD90^+/CD44^+/CD34^-/CD45^-$ (Figure S7, Supporting Information). As shown in Figure S8 (Supporting Information), no significant cytotoxicity is observed for either cell type when the concentration of NPs is below 20 μg mL^{-1}. Interestingly, the addition of 20 μg mL^{-1} or 40 μg mL^{-1} NPs facilitates 72 h proliferation of BMSCs to some extent, perhaps attributable to the release of Zn^{2+} from ZIF.[22] To validate the biological safety of NPs with a concentration of 20 μg mL^{-1}, the BMMs and BMSCs incubated with different NPs for 24 h and 72 h are examined by Live/Dead staining, and few dead cells with red fluorescence are observed from all the groups (**Figure 2**A,B). Therefore, a concentration of 20 μg ml^{-1} is selected for the subsequent cell experiments. The in vivo biosafety is determined using C57BL/6 mice, to which the samples are intravenously administrated with a concentration of 10 mg kg^{-1} every three days for up to three months. As revealed by hematoxylin and eosin (H&E) staining in Figure S9, Supporting Information, there is no obvious histological change in the major organs of each group. The erythrocyte hemolysis assay shows the hemolysis rates caused by different concentration of ZIF-H_2S-SDSSD NPs are all <1% (Figure 2C,D). These results indicate the NPs with or without H_2S-releasing properties have sufficient biocompatibility in vitro and in vivo.

NPs are easily incorporated into cells via different endocytic pathways and transported to lysosomes.[23] To verify the intracellular delivery of ZIF-H_2S-SDSSD NPs, BMMs, and BMSCs are incubated with C6-labeled NPs for different times. As shown in Figure 2E,F, after incubation for 4 h, significant colocalization of NPs (green) and lysosomal (red) is observed both in BMMs and BMSCs, indicating that ZIF-H_2S-SDSSD NPs are taken up into lysosomes, where they degrade to release Zn^{2+} and H_2S under acidic conditions.

2.4. Macrophage Reprogramming and Immuno-mediated Osteogenesis In Vitro

The immunomodulatory effects of the NPs are investigated on the BMMs with lipopolysaccharides (LPS) and interferon-γ (IFN-γ) stimulation. After different treatments, the cells are examined by immunofluorescence staining. As shown in **Figure 3**A–F, the decrease of M1 markers, inducible nitric oxide synthase (INOS), and CD86 as well as the increase of M2 markers, arginase 1 (ARG1), and CD206, are evident in the ZIF-H_2S and ZIF-H_2S-SDSSD groups. Flow cytometry validates that the ZIF-H_2S and ZIF-H_2S-SDSSD treatment can decrease the ratio of $F4/80^+/CD86^+$ cells (M1 phenotype) while elevating the ratio of $F4/80^+/CD206^+$ cells (M2 phenotype) (Figure 3G,H). Consistently, quantitative real-time polymerase chain reaction (RT-qPCR) analysis shows that the pro-inflammatory *Inos*, interleukin-1β (*Il-1*β), and *Il-6* are downregulated, while the anti-inflammatory *Arg1*, *Il-10* and transforming growth factor-β (*Tgf-*β) are upregulated by ZIF-H_2S and ZIF-H_2S-SDSSD intervention (Figure S10, Supporting Information). These results demonstrate the synergistic effects of Zn^{2+} and H_2S in reprogramming macrophages from the M1 phenotype to the M2 phenotype.

As the osteogenic differentiation of BMSCs is regulated by the immune microenvironment dominant with macrophages,[24] the conditioned medium (CM) is collected from BMMs in different groups to assess the immunomodulatory effects of various NPs on osteogenesis (Figure 3I). The enzyme-linked immunosorbent assay (ELISA) shows that CM obtained from the ZIF-H_2S and ZIF-H_2S-SDSSD groups contains less IL-1β and more IL-10, suggesting a potent inflammatory-attenuating effect through macrophage reprogramming (Figure 3J,K). On day 7 of osteogenic induction with CM, the BMSCs from the ZIF-H_2S and ZIF-H_2S-SDSSD groups exhibit a higher osteocalcin (OCN) expression than the other groups (Figure 3L,M). In the meantime, the alkaline phosphatase (ALP) activity of

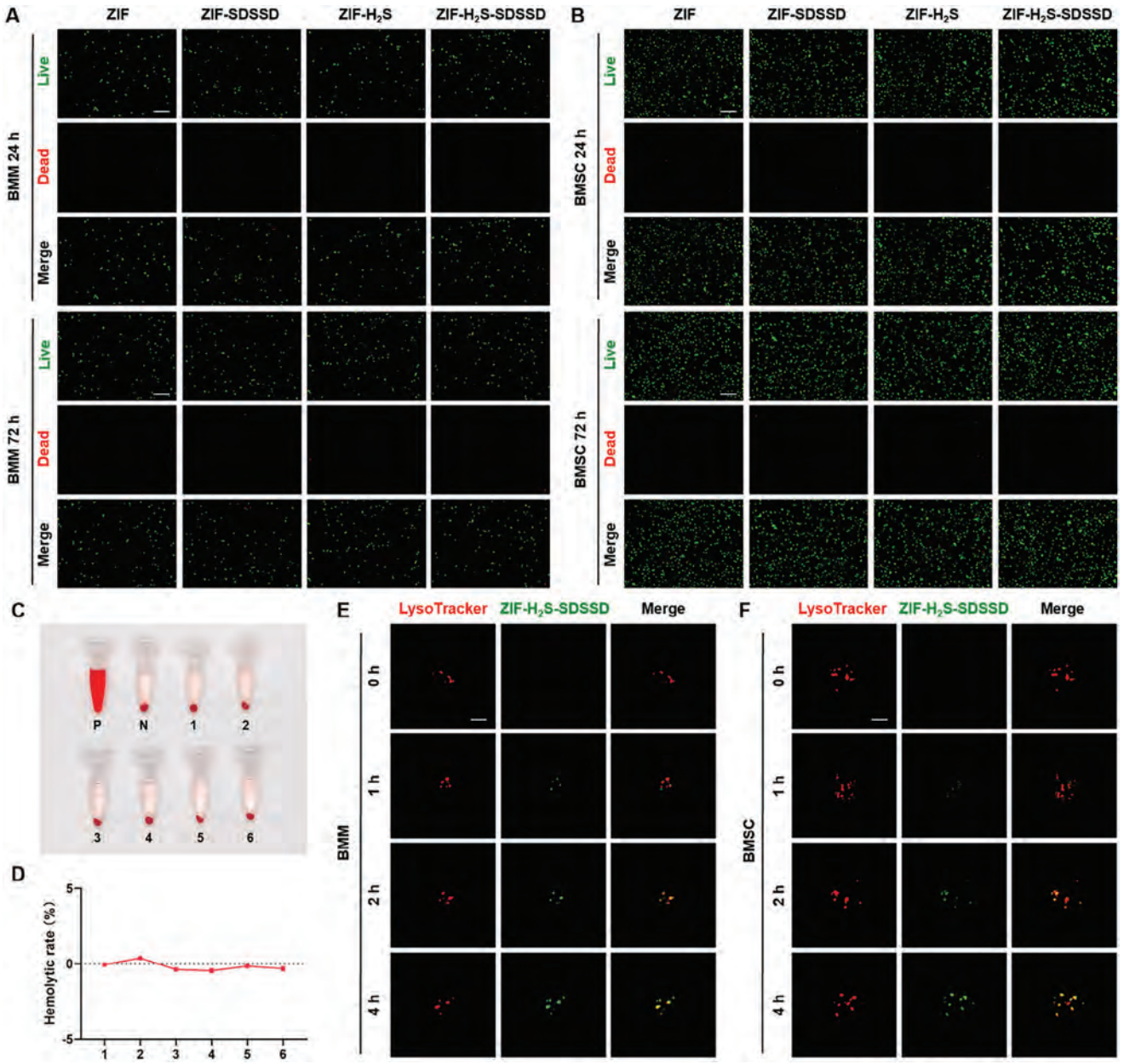

Figure 2. Biocompatibility of different NPs. A,B) Live/dead staining of BMMs and BMSCs incubated with different NPs with a concentration of 20 μg mL^{-1} for 24 and 72 h (scale bar = 200 μm). C,D) Erythrocyte hemolysis assay and quantitative analysis of hemolytic rate of different groups, including positive control (P), negative control (N), and ZIF-H_2S-SDSSD NPs with a concentration of 5 (1), 10 (2), 20 (3), 40 (4), 80 (5), and 160 μg mL^{-1} (6) (n = 3 per group). E,F) Fluorescence images of BMMs and BMSCs incubated with ZIF-H_2S-SDSSD (green) and LysoTracker (red) for different times (scale bar = 10 μm). The data are presented as the mean ± SD.

CM-treated BMSCs is upregulated when ZIF-H_2S and ZIF-H_2S-SDSSD NPs are involved (Figure 3N,O,Q). After culturing BMSCs with CM for 14 days, alizarin red S (ARS) staining is carried out. The ZIF-H_2S and ZIF-H_2S-SDSSD groups exhibit more red-stained calcium deposits than the other groups (Figure 3P,R). Furthermore, RT-qPCR analysis reveals an increased expression of osteogenesis-related genes, such as runt-related transcription factor 2 (*Runx2*), osterix (*Sp7*), *Ocn*, and osteopontin (*Opn*), in the ZIF-H_2S and ZIF-H_2S-SDSSD groups (Figure S11, Supporting Information). Overall, the combination of Zn^{2+} and H_2S facilitates immuno-mediated osteogenesis by macrophage reprogramming.

The immunomodulatory effects of NPs on osteoclast formation are also investigated. On day 5 of osteoclastic induction using CM collected from BMMs in various groups, both F-actin ring staining and tartrate-resistant acid phosphatase (TRAP) staining of osteoclasts in ZIF-H_2S-SDSSD group are decreased compared with the other groups, whereas this difference is not statistically significant (Figure S12, Supporting Information). These results suggest that the immunomodulatory effects of ZIF-H_2S-SDSSD

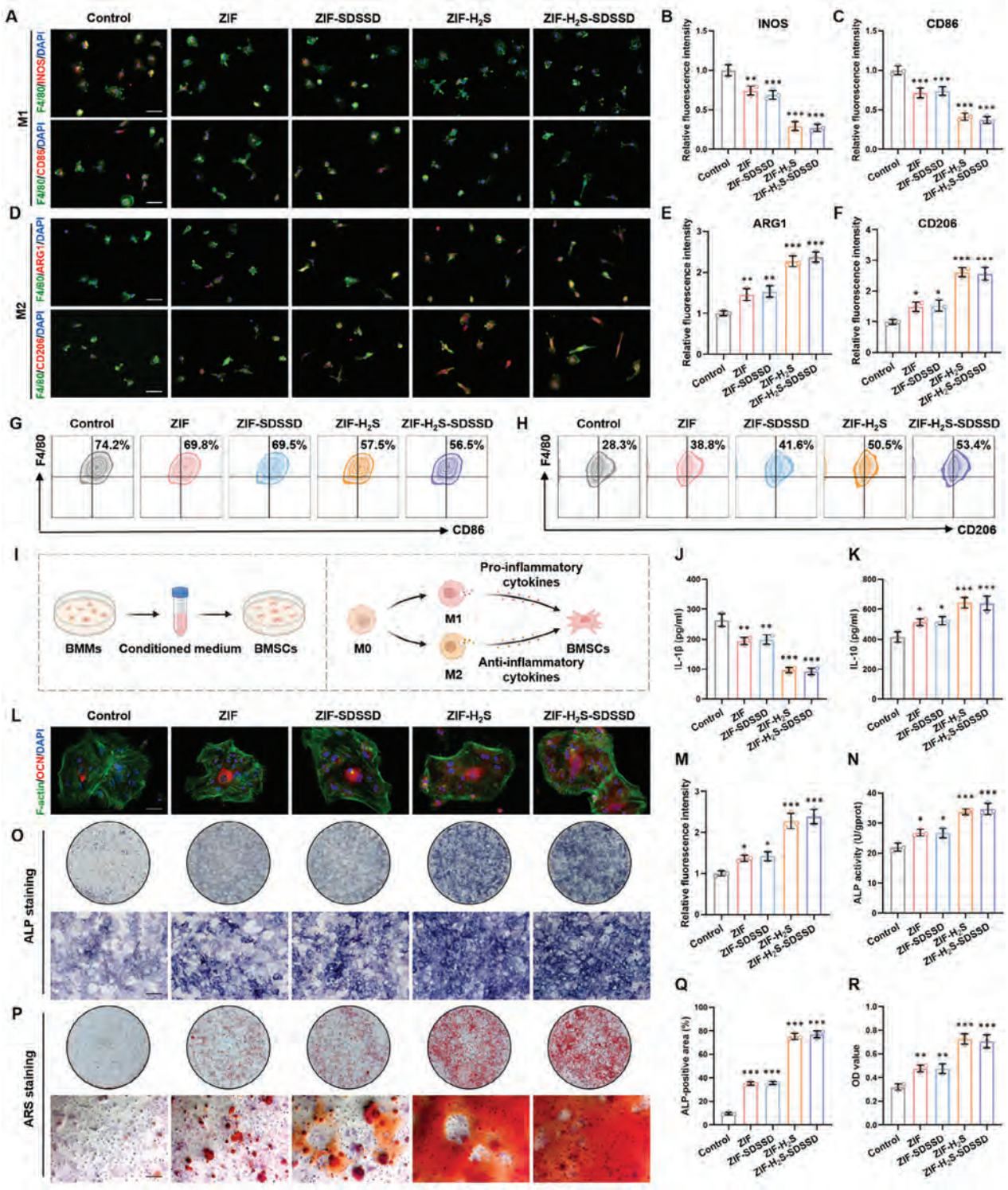

Figure 3. Macrophage reprogramming and immuno-mediated osteogenesis in vitro. A–F) Immunofluorescence staining images and quantitative evaluation of BMMs after different treatments (green: F4/80, red: M1 macrophage markers INOS or CD86 and M2 macrophage markers ARG1 or CD206, blue: DAPI, scale bar = 50 μm, $n = 3$ per group). G,H) The proportion of $F4/80^+/CD86^+$ and $F4/80^+/CD206^+$ BMMs determined by flow cytometry ($n = 3$ per group). I) Schematic illustration of the experimental design of immuno-modulated osteogenesis. J,K) Secreted IL-1β and IL-10 in CM detected by ELISA. L,M) Immunofluorescence staining images and quantitative evaluation of BMSCs cultured with different CM (green: F-actin, red: OCN, blue: DAPI, scale bar = 50 μm, $n = 3$ per group). N) ALP activity assay ($n = 3$ per group). O,Q) ALP staining images and quantitative evaluation (scale bar = 200 μm, $n = 3$ per group). P,R) ARS staining images and quantitative evaluation (scale bar = 100 μm, $n = 3$ per group). The data are presented as mean ± SD. Statistical analysis is performed by one-way ANOVA with Tukey's test. Compared with the control group, $^*p < 0.05$, $^{**}p < 0.01$, $^{***}p < 0.001$.

NPs on osteoclastogenesis through macrophage reprogramming can be negligible.

2.5. Immunoregulatory Mechanism of ZIF-H_2S-SDSSD NPs

To elucidate the immunoregulatory mechanism of ZIF-H_2S-SDSSD NPs, transcriptome sequencing, and metabolomic analysis are conducted on the LPS/IFN-γ stimulated BMMs with or without ZIF-H_2S-SDSSD intervention. Principal component analysis (PCA) shows that the samples meet the requirements of quality control as well as a clear separation between the two groups (Figure S13A, Supporting Information). The volcano plot of differentially expressed genes (DEGs) reveals 2065 up-regulated genes and 2204 down-regulated genes by comparing the ZIF-H_2S-SDSSD group with the control group (**Figure** 4A). Gene ontology (GO) enrichment analysis highlights that these DEGs are predominantly involved in the metabolic processes (Figure 4B). Meanwhile, the Kyoto encyclopedia of genes and genomes (KEGG) enrichment analysis indicates that inflammatory macrophage activation-related pathways are downregulated in the ZIF-H_2S-SDSSD group, including the tumor necrosis factor (TNF) signaling pathway, toll-like receptor signaling pathway, hypoxia-inducible factor 1 (HIF-1) signaling pathway, nucleotide-binding oligomerization domain (NOD)-like receptor signaling pathway, and nuclear factor-kappa B (NF-kappa B) signaling pathway (Figure 4C). Consistently, gene set enrichment analysis (GSEA) shows a negative correlation with the TNF signaling pathway in the ZIF-H_2S-SDSSD group (Figure 4D). The heat map illustrating DEGs related to macrophage polarization also indicates the transition from the M1 phenotype to the M2 phenotype in response to ZIF-H_2S-SDSSD intervention (Figure S13B, Supporting Information).

Further metabolomic analysis reveals that the metabolites involved in the glycolysis and tricarboxylic acid (TCA) cycle undergo significant changes after ZIF-H_2S-SDSSD treatment. As shown in Figure 4E,H, the key products of glycolysis, such as fructose 6-phosphate, fructose 1, 6-bisphosphate, glyceraldehyde 3-phosphate, dihydroxyacetone phosphate, phosphoenol pyruvic acid, and pyruvic acid, decrease in the ZIF-H_2S-SDSSD group, whereas several intermediates in the TCA cycle including citrate, α-ketoglutarate, fumarate, malate, and oxaloacetate increase. Interestingly, a lower level of succinate is observed, indicating a break in the TCA cycle.[25] These results suggest that ZIF-H_2S-SDSSD alters the metabolic profiles of incubated macrophages. Seahorse extracellular flux analysis is performed to verify the metabolomic results. The real-time extracellular acidification rate (ECAR) and oxygen consumption rate (OCR) are determined during sequential drug additions. As shown in Figure 4F,G, the glycolysis, glycolytic capacity, and glycolytic reserve decrease significantly, whereas the basal respiration, ATP production, maximal respiration, and spare respiratory capacity rise after the ZIF-H_2S-SDSSD treatment (Figure 4I,J). These results demonstrate that ZIF-H_2S-SDSSD NPs inhibit glycolysis while promoting the TCA cycle and cellular respiration. The reduced basal respiration in the control group can be attributed to the loss of mitochondrial fitness, as indicated by the reduced maximal respiration.[26]

The decreased mitochondrial membrane potential ($\Delta\psi$m) is a marker of mitochondrial dysfunction.[27] To evaluate whether the metabolic reprogramming of macrophages results from abnormal mitochondrial functions, $\Delta\psi$m is detected by the JC-1 probe. When $\Delta\psi$m is normal, JC-1 forms aggregates (red) in the matrix of mitochondria. In contrast, JC-1 exists as monomers (green) under the condition with reduced $\Delta\psi$m. As shown in Figure 4K, the proportion of monomers^{+high} / aggregates^{+low} cells in the ZIF-H_2S-SDSSD group is lower than that of the control group, suggesting that dysfunctional mitochondria decrease in response to ZIF-H_2S-SDSSD intervention. It has been reported that the loss of $\Delta\psi$m is associated with the accumulation of mitochondrial ROS (mtROS).[28] Hence, the mtROS level is assessed using a mitochondria-specific ROS indicator, MitoSOX. As shown in Figure 4L, the mtROS level indicated by MitoSOX fluorescence of the ZIF-H_2S-SDSSD group decreases. These findings suggest that H_2S released from ZIF-H_2S-SDSSD NPs acts as a potent antioxidant to protect mitochondria by scavenging mtROS, thus promoting metabolic reprogramming of macrophages by inhibiting mitochondrial dysfunction caused by mtROS.

The accumulation of succinate is essential for the inflammatory activation of macrophages, which stabilizes HIF-1α by inhibiting the function of prolyl hydroxylase (PHD). The activation of HIF-1α further promotes glycolysis and IL-1β production, thus mediating macrophages toward the inflammatory phenotype.[29] Liquid chromatography-mass spectrometry (LC-MS) shows a significant reduction of succinate level in the ZIF-H_2S-SDSSD group compared with the control group (Figure S13C, Supporting Information). Immunofluorescence staining shows that the HIF-1α and IL-1β expressions of BMMs decrease following the treatment with ZIF-H_2S-SDSSD NPs, consistent with the reduced succinate accumulation (Figure 4M,N). Notably, succinate can be oxidized by succinate dehydrogenase to drive extensive mtROS production, which induces HIF-1α expression via the NF-κB pathway.[30] Therefore, the reduction of mtROS in macrophages after the ZIF-H_2S-SDSSD treatment is partially related to the decreased succinate accumulation. Overall, these findings indicate that ZIF-H_2S-SDSSD NPs can promote macrophage metabolic reprogramming by suppressing succinate accumulation and mtROS production, which suppresses the inflammatory phenotype of macrophages by inhibiting the succinate/HIF-1α/IL-1β signaling pathway (Figure 4O).

2.6. Osteoblast-Osteoclast Coupling In Vitro

Osteoblast-osteoclast coupling plays a predominant role in the healing process of osteoporotic fracture, primarily through the enhancement of osteogenesis and the suppression of osteoclastogenesis under osteoporotic conditions.[31] Hence, the direct effect of various NPs on the osteogenic differentiation of BMSCs is investigated in vitro. On day 7 after osteogenic induction, the highest OCN and ALP expressions are detected in ZIF-H_2S and ZIF-H_2S-SDSSD groups (**Figure** 5A–E). After osteogenic induction of BMSCs for 14 days, the ZIF-H_2S and ZIF-H_2S-SDSSD groups exhibit more red-stained calcium deposits than the other groups (Figure 5F,G). Furthermore, RT-qPCR analysis reveals that ZIF-H_2S and ZIF-H_2S-SDSSD upregulate the expressions of osteogenesis-related genes, including *Runx2, Sp7, Ocn*, and *Opn*, in BMSCs (Figure S14, Supporting Information). These results indicate the desirable effects of

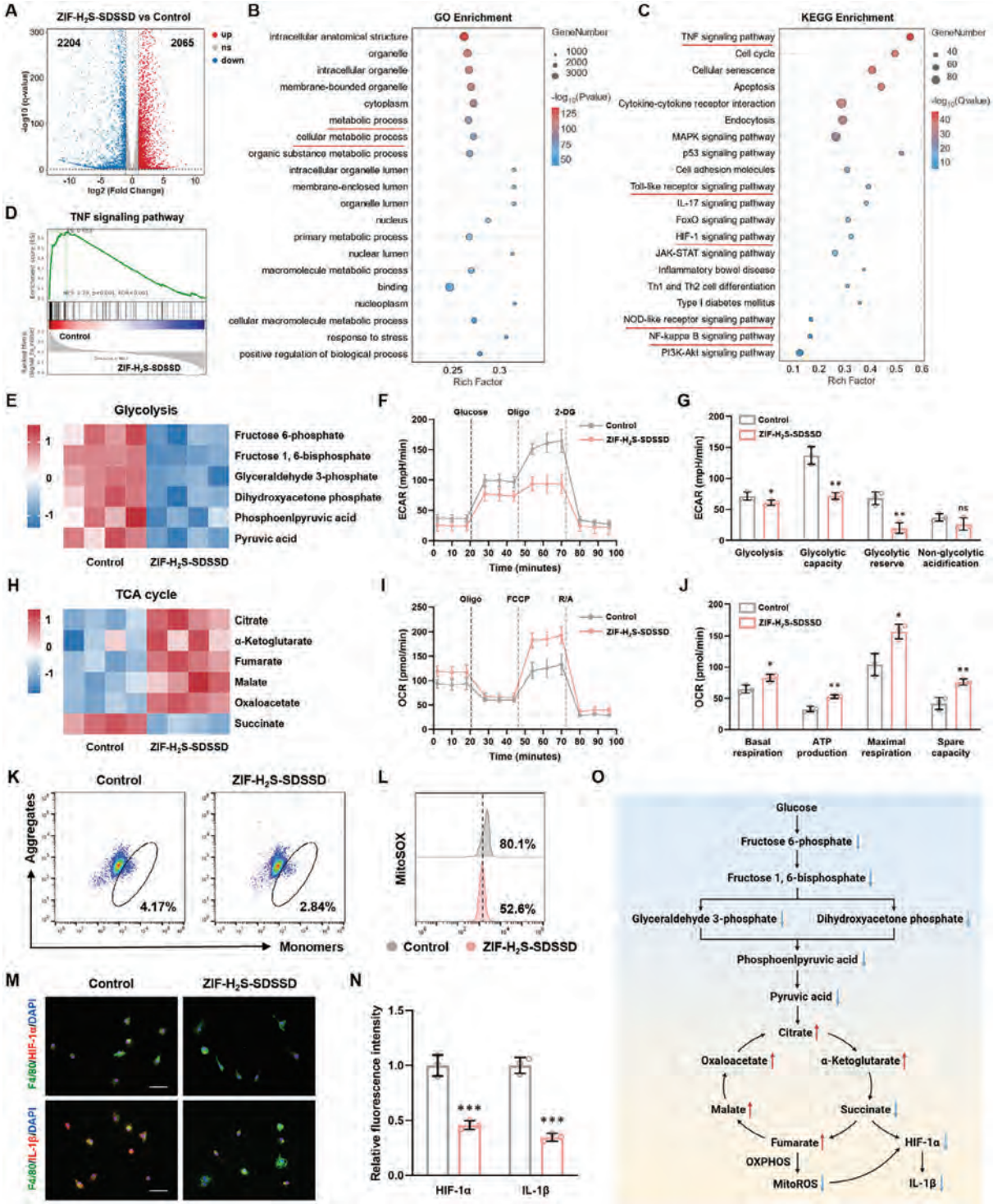

Figure 4. Immunoregulatory mechanism of ZIF-H_2S-SDSSD NPs. A) Volcano plot of DEGs (q values < 0.05 and |log2foldchange| > 1). B) GO enrichment analysis. C) KEGG enrichment analysis. D) GSEA of TNF signaling pathway. E) Heatmaps of metabolites involved in glycolysis ($n = 4$ per group). F,G) Real-time ECAR of BMMs in the glycolytic stress assay and quantitative evaluation ($n = 3$ per group). H) Heatmaps of metabolites involved in the TCA cycle ($n = 4$ per group). I,J) Real-time OCR of BMMs in the mitochondrial stress assay and quantitative evaluation ($n = 3$ per group). K) The proportion of JC-1 monomers^{+high} / aggregates^{+low} BMMs determined by flow cytometry. L) Content of mitoSOX in BMMs determined by flow cytometry. M,N) Immunofluorescence staining images and quantitative evaluation of BMMs with or without ZIF-H_2S-SDSSD treatment (Green: F4/80, red: HIF-1α or IL-1β, blue: DAPI, scale bar = 50 μm, $n = 3$ per group). O) Schematic illustration of the immunoregulatory mechanism of ZIF-H_2S-SDSSD NPs. The data are presented as mean ± SD. Statistical analysis is performed by the unpaired Student's t-test. Compared with the control group, ns indicates no significant difference, *$p < 0.05$, **$p < 0.01$, ***$p < 0.001$.

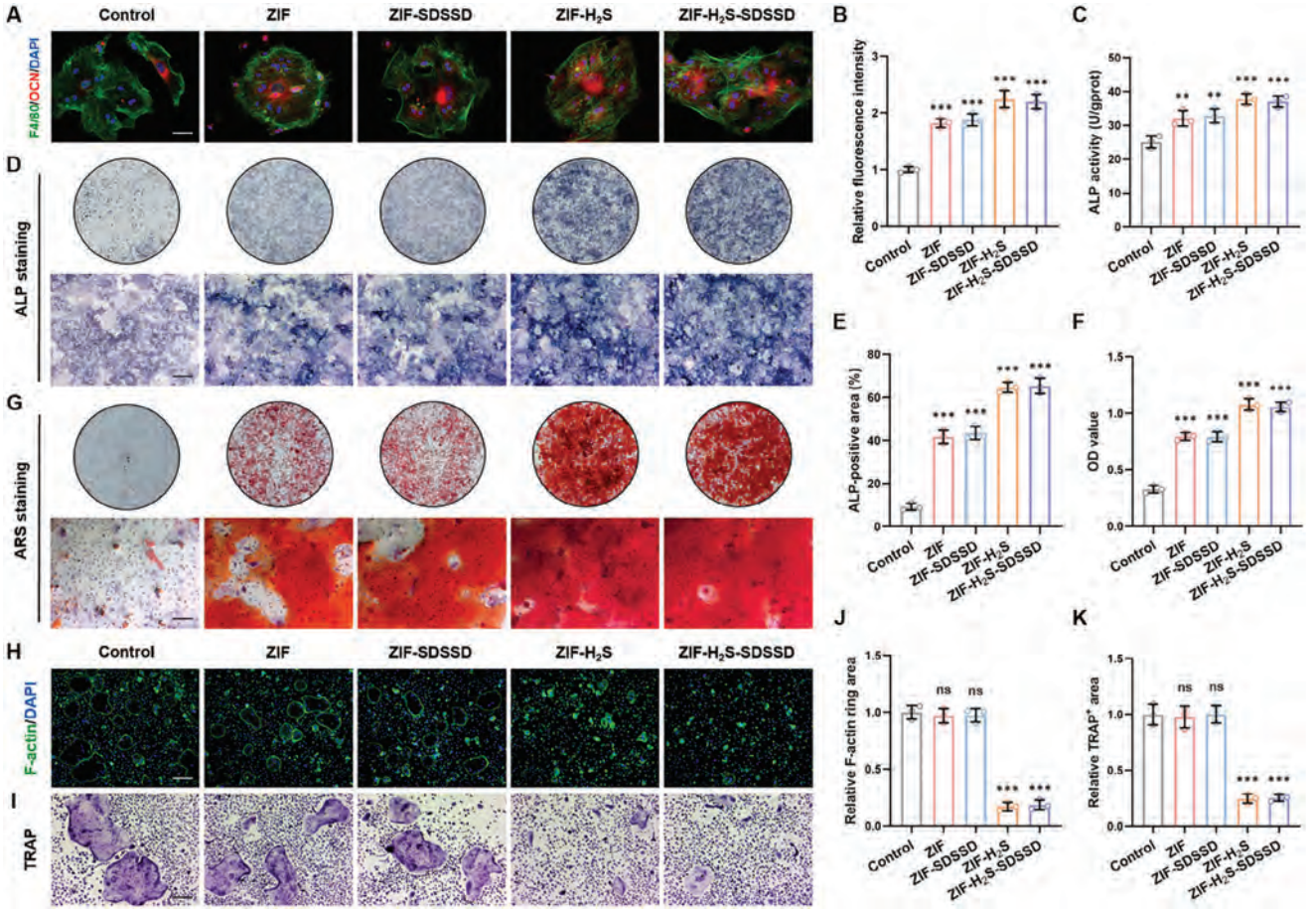

Figure 5. Regulation of osteoblast-osteoclast coupling in vitro. A,B) Immunofluorescence staining images and quantitative evaluation of BMSCs after different treatments (green: F-actin, red: OCN, blue: DAPI, scale bar = 50 μm, $n = 3$ per group). C) ALP activity assay ($n = 3$ per group). D,E) ALP staining images and quantitative evaluation (scale bar = 200 μm, $n = 3$ per group). F,G) ARS staining images and quantitative evaluation (scale bar = 100 μm, $n = 3$ per group). H,J) F-actin ring staining images and quantitative evaluation of osteoclasts after different treatments (green: F-actin, blue: DAPI, scale bar = 200 μm, $n = 3$ per group). I,K) TRAP staining images and quantitative evaluation (scale bar = 100 μm, $n = 3$ per group). The data are presented as the mean ± SD. Statistical analysis is performed by one-way ANOVA with Tukey's test. Compared with the control group, ns indicates no significant difference, $^{**}p < 0.01$, $^{***}p < 0.001$.

ZIF-H_2S and ZIF-H_2S-SDSSD NPs on promoting the osteogenic differentiation of BMSCs, which is consistent with previous studies.[32]

In the next step, the direct effect of various NPs on osteoclastogenesis is investigated in vitro. On day 5 of osteoclastic induction, the F-actin ring area of osteoclasts incubated with ZIF and ZIF-SDSSD NPs shows no difference with the control group, whereas a significant decrease of F-actin ring area is observed in the ZIF-H_2S and ZIF-H_2S-SDSSD groups (Figure 5H,J). Similarly, TRAP staining indicates that ZIF-H_2S and ZIF-H_2S-SDSSD NPs can reduce the TRAP-positive area of the cultured cells (Figure 5I,K). The expressions of osteoclastogenesis-related genes including cathepsin k (*Ctsk*), matrix metallopeptidase 9 (*Mmp9*), nuclear factor of activated T cells 1 (*Nfatc1*), and ATPase H^+ transporting v0 subunit d2 (*Atp6v0d2*) are investigated by RT-qPCR, which are down-regulated in the ZIF-H_2S and ZIF-H_2S-SDSSD groups (Figure S15, Supporting Information). Collectively, the inhibitory effect of ZIF-H_2S and ZIF-H_2S-SDSSD NPs on osteoclastogenesis is demonstrated. Although whether inhibiting osteoclastic differentiation facilitates fracture healing remains controversial,[33] the suppression of osteoclastogenesis can undoubtedly alleviate bone loss and prevent recurrent osteoporotic fractures.

2.7. Bone-Targeting Capability of ZIF-H_2S-SDSSD NPs In Vivo

The SDSSD peptide has been shown to target bone by binding periostin (POSTN), an extracellular matrix protein widely present in bone tissue.[34] Prior to the in vivo study, the POSTN expression of different experimental mice is assessed by immunohistochemical staining. As shown in Figure S16, Supporting Information, POSTN is highly expressed in the callus and trabeculae regions of both the normal mice and OVX mice. No significant difference is observed between the two groups, indicating that SDSSD is suitable for the bone-targeting modification of NPs for osteoporotic fracture. To investigate the bone-targeting performances in vivo, the experimental mice with osteoporotic fracture are intravenously injected with Cy7-labeled ZIF-H_2S-SDSSD NPs

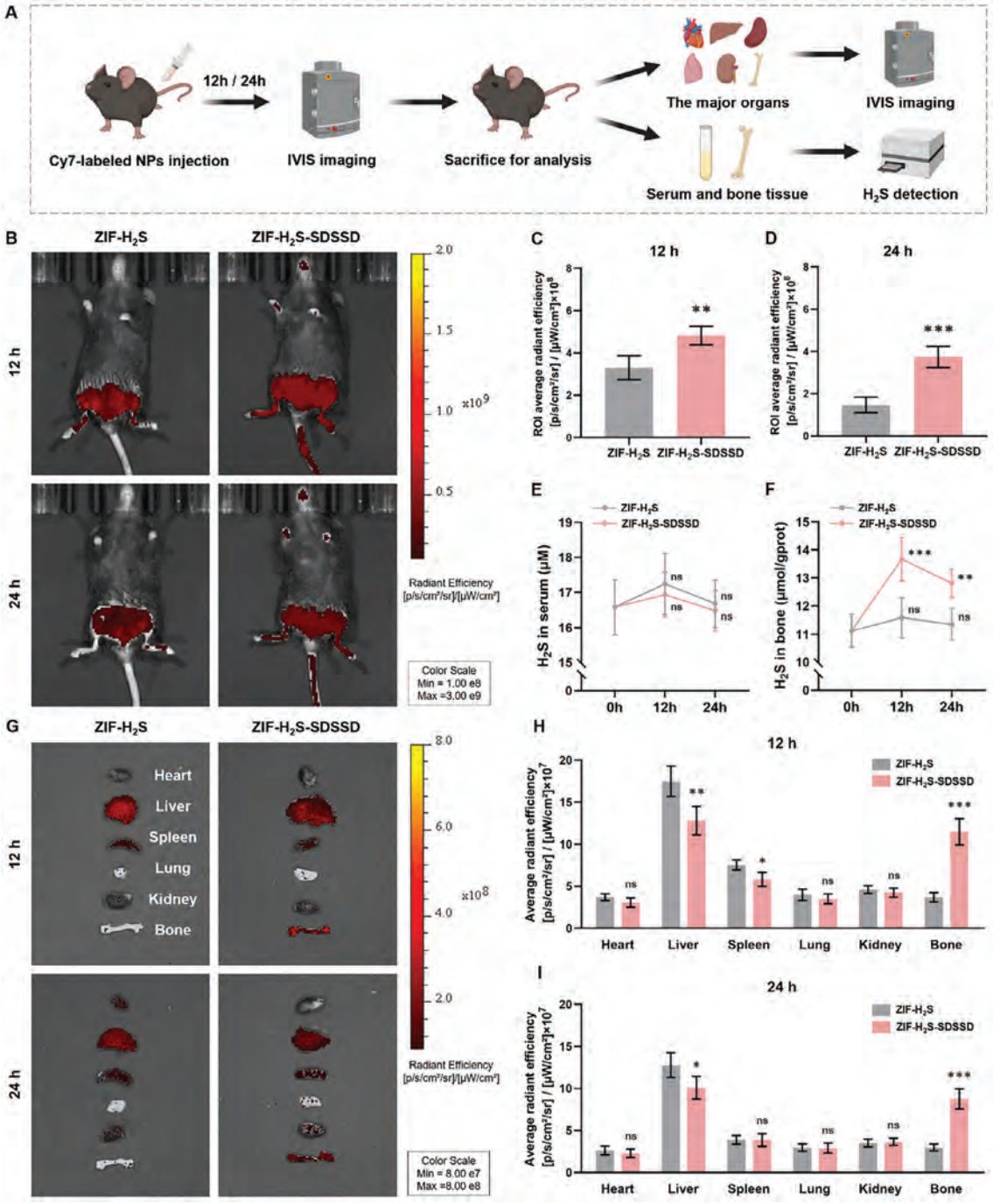

Figure 6. Bone-targeting properties of ZIF-H_2S-SDSSD NPs in vivo. A) Schematic illustration of the in vivo bone-targeting experiments. B–D) IVIS imaging of mice and quantitative evaluation of radiant efficiency in the region of interest. E,F) H_2S concentration in serum and bone of mice ($n = 4$ per group). G–I) Fluorescent imaging of major organs and quantitative evaluation of radiant efficiency ($n = 4$ per group). The data are presented as mean ± SD. Statistical analysis is performed by the unpaired Student's *t*-test. Compared with the ZIF-H_2S group (Figure C, D, H, I) or the 0 h group (Figure E, F), ns indicates no significant difference, $*p < 0.05$, $**p < 0.01$, $***p < 0.001$.

(targeted group) and Cy7-labeled ZIF-H_2S NPs (non-targeted group), respectively. The biodistributions in vivo are tracked by in vivo imaging system (IVIS), and the serum and bone tissue of mice are harvested for H_2S detection (**Figure** 6A). At 12 h and 24 h after administration, whole-body fluorescent imaging shows the Cy7-labeled ZIF-H_2S-SDSSD NPs exhibit high accumulation in bone tissue (Figure 6B–D). In the ZIF-H_2S group, the H_2S levels in both serum and bone remain unchanged at 12 h and 24 h post-injection. In contrast, the H_2S level in bone increases significantly in the ZIF-H_2S-SDSSD group at both time

points, while that detected in serum is stable (Figure 6E,F). Compared with the ZIF-H_2S group, stronger fluorescent signals are observed from the bone tissues of the ZIF-H_2S-SDSSD group, indicating that SDSSD modification promotes bone accumulation of NPs (Figure 6G–I). These results demonstrate that ZIF-H_2S-SDSSD NPs possess the bone-targeting capability to increase the H_2S concentration in bone tissue without affecting the serum H_2S concentration, thereby mitigating the potential risks of systematic H_2S delivery.

2.8. Osteoporotic Fracture Healing and Alleviation of Osteoporosis In Vivo

The therapeutic effects of ZIF-H_2S-SDSSD NPs are investigated in vivo based on an osteoporotic fracture mice model. Fracture healing is evaluated with the fractured left femur, and amelioration of osteoporosis is assessed with the uninjured right femur. To minimize interferences with the recruitment of neutrophils and monocytes in the early inflammatory stages of fracture healing, the NPs are administrated 48 h after fracture surgery.[9] ZIF NPs, ZIF-SDSSD NPs, ZIF-H_2S NPs, and ZIF-H_2S-SDSSD NPs with a concentration of 10 mg kg^{-1}, along with normal saline, are injected intravenously every three days. X-ray imaging is performed to confirm fracture fixation, and the mice are sacrificed on the 7th, 14th, and 28th day after fracture surgery for further evaluation (**Figure** 7A,B). The H_2S concentration in the serum and bone tissues is determined to assess the H_2S delivery capability of various NPs. As shown in Figure 7C,D, the ZIF-H_2S-SDSSD group shows a higher H_2S level in the bone tissue on day 7 and day 28, whereas the serum H_2S level is not affected. However, the H_2S level in the bone tissue of the ZIF-H_2S-SDSSD group does not change significantly on the 14th day. This discrepancy can be attributed to the longer interval between the most recent NPs injection and H_2S detection on day 14 than that on day 7 and day 28. These results indicate that ZIF-H_2S-SDSSD NPs can increase the H_2S level in the bone tissue without affecting the serum H_2S concentration, and the results are consistent with the bone-targeting results described above.

Micro-CT scanning is performed on the femurs to assess the therapeutic efficacy of ZIF-H_2S-SDSSD NPs on osteoporotic fracture. As shown in Figure 7E,F, the ZIF-H_2S-SDSSD group exhibits a higher callus index than the normal saline group on the 7th and 14th day post-surgery, indicative of the formation of larger callus. On the 28th day post-surgery, the callus index of the ZIF-H_2S-SDSSD group is lower than that of the other groups, reflecting an earlier initiation of the callus modification phase. Bone parameter analysis shows the callus BV/TV of the ZIF-H_2S-SDSSD group is the highest at all three time points (Figure 7G). Meanwhile, the trabeculae under the distal femur growth plate of the unfractured right femur are analyzed to evaluate the progression of osteoporosis. Bone parameter analysis including BV/TV, BS/TV, Tb.N, and Tb.Sp demonstrates serious bone loss caused by OVX in the normal saline group, whereas the degenerative change is mitigated by NPs administration, especially in the ZIF-H_2S-SDSSD group (Figure S17, Supporting Information). These results indicate that the administration of ZIF-H_2S-SDSSD NPs effectively promotes osteoporotic fracture healing and alleviates osteoporosis in vivo.

Histological staining is carried out to confirm the therapeutic effects of ZIF-H_2S-SDSSD NPs on osteoporotic fracture. The results of H&E staining and Masson staining reveal that the ZIF-H_2S-SDSSD group provides the largest callus area and most newly formed bone on the 14th day (**Figure** 8A–D). On the 28th day post-surgery, the callus area of the ZIF-H_2S-SDSSD group is smaller than those of the other groups. The results suggest an earlier initiation of the callus modification phase in the ZIF-H_2S-SDSSD group, which is consistent with the better histological morphology observed on the 28th day. TRAP staining discloses significantly fewer TRAP-positive osteoclasts after the ZIF-H_2S-SDSSD treatment, indicative of the suppression of osteoclastogenesis (Figure 8E,F). Considering the predominance of macrophages in the initial healing period of fracture, the polarization of macrophages in the callus is analyzed by immunofluorescence and immunohistochemical staining on the 7th day after surgery. Compared with the normal saline group, the ZIF-H_2S-SDSSD group shows less F4/80$^+$/CD86$^+$ cells and more F4/80$^+$/CD206$^+$ cells (Figure 8G–I). Consistently, the expression of IL-1β is reduced while the level of IL-10 is elevated after the administration of ZIF-H_2S-SDSSD NPs, indicating an inhibitory effect on inflammation (Figure 8J–L). Furthermore, H&E staining, Masson staining, and TRAP staining are performed on the trabeculae under the distal femur growth plate on the 28th day post-surgery. The ZIF-H_2S-SDSSD group exhibits more trabeculae and newly formed bone associated with the reduced TRAP-positive osteoclasts (Figure S18, Supporting Information). Overall, ZIF-H_2S-SDSSD NPs can simultaneously promote fracture healing and mitigate osteoporosis, thus holding great promise in the postoperative treatment of osteoporotic fracture.

The therapeutic effects of ZIF-H_2S-SDSSD NPs on normal fracture were also investigated in mice without osteoporosis. Micro-CT measurements of BV/TV of fracture callus indicated that ZIF-H_2S-SDSSD NPs effectively facilitated the normal fracture healing (Figure S19, Supporting Information). Owing to the extensive effects of Zn^{2+} and H_2S on bone tissue microenvironment, ZIF-H_2S-SDSSD NPs are expected to be used in the treatment of other orthopedic diseases and have broad application prospects in this field.

3. Conclusion

In this study, multifunctional ZIF-H_2S-SDSSD NPs are constructed by encapsulating zinc sulfide in ZIF and functionalizing the surface of NPs with SDSSD peptide. The bone-targeting property of ZIF-H_2S-SDSSD NPs is desirable for systematic H_2S delivery. Upon cellular uptake, the acidic environment in lysosomes drives the release of H_2S from the acid-labile zinc sulfide along with the degradation of ZIF. The synergistic effects of Zn^{2+} and H_2S promote macrophage metabolic reprogramming by suppressing succinate accumulation and mtROS production, and further regulate osteoblast-osteoclast coupling. Intravenous administration of ZIF-H_2S-SDSSD NPs can effectively accelerate fracture healing and increase bone mass without noticeable side effects. Overall, this strategy holds great promise in the clinical treatment of osteoporotic fracture and provides insights into the development of nanomedicine therapy for orthopedic diseases.

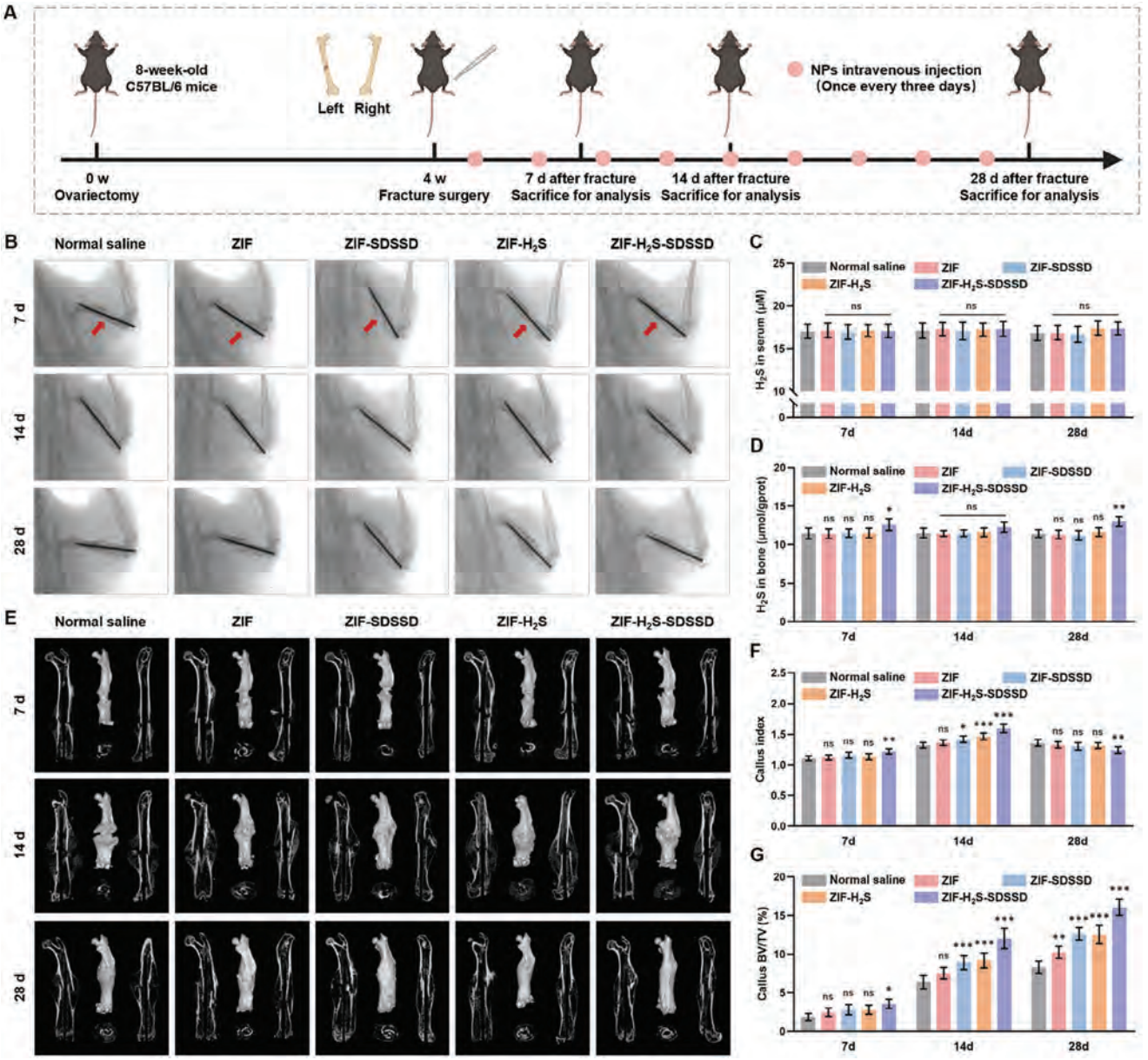

Figure 7. Therapeutic effects of osteoporotic fracture in vivo. A) Schematic illustration of the in vivo experiments. B) Representative images of X-ray imaging (Red arrows indicate fracture gaps). C,D) H_2S concentration in serum and bone tissues of mice ($n = 5$ per group). E) Representative images of micro-CT and 3D reconstruction of femur osteoporotic fracture after different treatments. F,G) Micro-CT measurements of callus index and BV/TV of fracture callus ($n = 5$ per group). The data are presented as mean ± SD. Statistical analysis is performed by one-way ANOVA with Tukey's test. Compared with the normal saline group, ns indicates no significant difference, $*p < 0.05$, $**p < 0.01$, $***p < 0.001$.

4. Experimental Section

Synthesis of ZIF and ZIF-H_2S NPs: The ZIF NPs were synthesized by gradually mixing 1 ml of the $Zn(NO_3)_2{\cdot}6H_2O$ (250 mg) solution in methanol with 1 ml of deionized water and 10 ml of the 2-MIM (2.8375 g) solution in methanol. The mixture was stirred at room temperature for 30 min. The precipitate was collected by centrifugation at 8000 g for 5 min and washed three times with methanol. The ZIF NPs were dispersed in methanol for further characterization. The ZIF-H_2S NPs were synthesized following a similar protocol, except that 1 ml of deionized water was replaced with 1 ml of the NaHS solution (12.5 mM) in deionized water.

Synthesis of ZIF-SDSSD and ZIF-H_2S-SDSSD NPs: Cysteine was coupled to the bone-targeting peptide SDSSD to provide the thiol functionality. The peptide was dissolved into water and diluted with methanol to a final concentration of 0.1 mg ml^{-1}. The prepared ZIF and ZIF-H_2S NPs were resuspended in the peptide solution with a concentration of 3 mg ml^{-1}. The mixture was stirred at room temperature for 30 min, and the product was collected by centrifugation and washed three times with methanol.

Characterization of NPs: The morphology of the NPs was observed by SEM (SU8010, Hitachi, Japan) at an accelerating voltage of 3.0 kV. The TEM images were acquired on a Talos F200 equipped with EDS (Thermo Fisher, USA). The particle size distribution and zeta potentials in

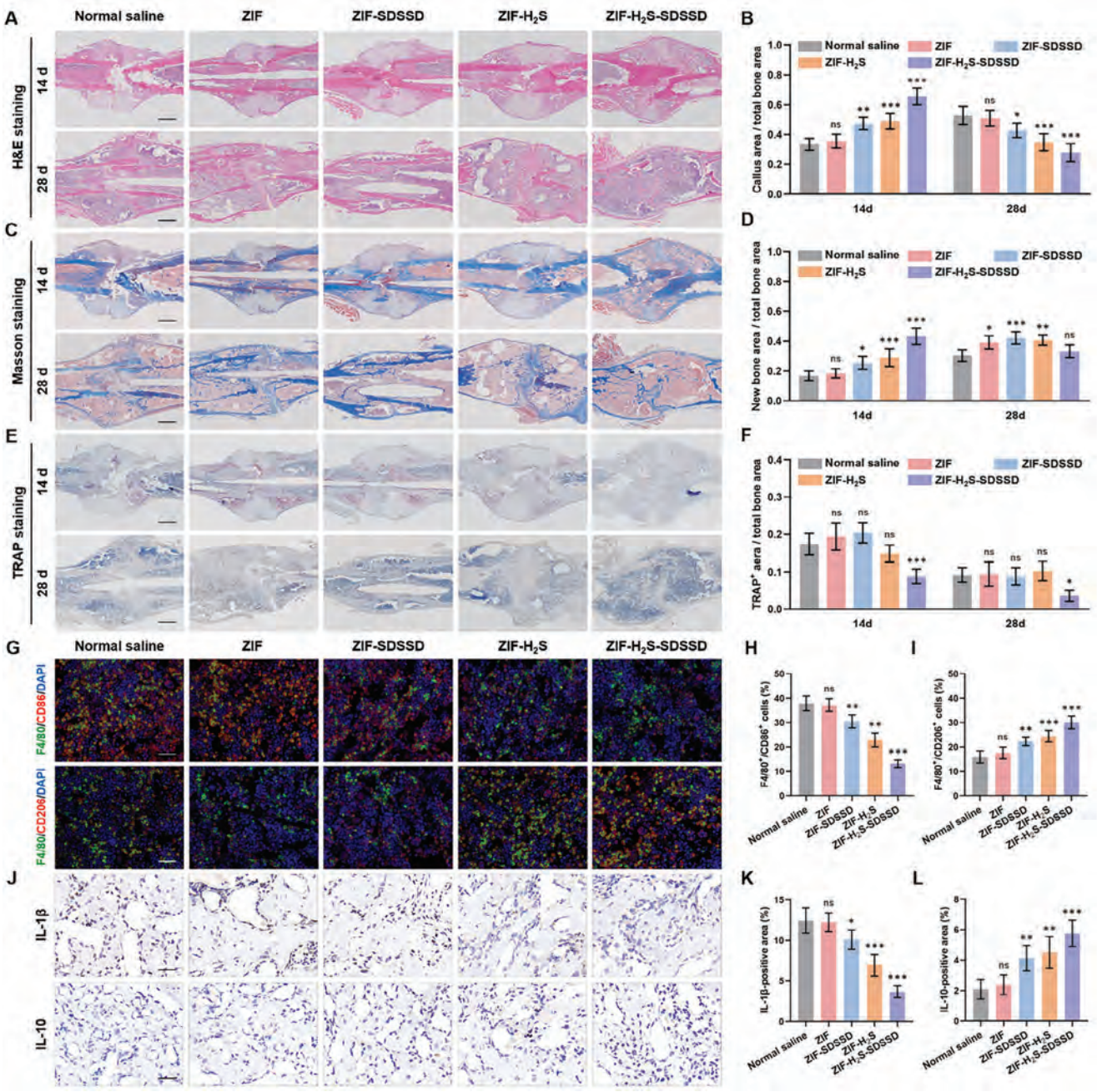

Figure 8. Histological staining of fracture callus. A,B) H&E staining and quantitative evaluation of fracture callus on day 14 and day 28 post-surgery (scale bar = 500 μm, $n = 5$ per group). C,D) Masson staining and quantitative evaluation of fracture callus on the 14th and 28th day after surgery (scale bar = 500 μm, $n = 5$ per group). E,F) TRAP staining and quantitative evaluation of fracture callus on day 14 and day 28 post-surgery (scale bar = 500 μm, $n = 5$ per group). G–I) Immunofluorescence staining and quantitative evaluation of fracture callus on day 7 post-surgery (green: F4/80, red: M1 macrophages markers CD86 and M2 macrophages markers CD206, blue: DAPI, scale bar = 100 μm, $n = 5$ per group). J–L) Immunohistochemical staining and quantitative evaluation of IL-1β and IL-10 in fracture callus on day 7 post-surgery (scale bar = 100 μm, $n = 5$ per group). The data are presented as the mean ± SD. Statistical analysis is performed by one-way ANOVA with Tukey's test. Compared with the normal saline group, ns indicates no significant difference, $*p < 0.05$, $**p < 0.01$, $***p < 0.001$.

deionized water were measured on the ZSU3100 instrument (Malvern Panalytical, UK). The BET surface area and micropore volume were determined by measuring the N_2 adsorption-desorption isotherms at 77 K on the ASAP2460 analyzer (Micromeritics, USA). The phase of the NPs was analyzed by X-ray diffraction (XRD) with Cu K_α ($\lambda = 1.5406$ Å) radiation on a D8 ADVANCE diffractometer (Bruker, Germany), and X-ray photoelectron spectroscopy (XPS) was conducted on the ESCALAB 250XI (Thermo Fisher, USA).

The concentration of the SDSSD peptide solution was determined by a BCA protein assay kit (Thermo Fisher, USA). A standard concentration

curve was established by spectrophotometric analysis at 562 nm. The nominal concentration of SDSSD peptide grafted on NPs was determined by allowing the ZIF-SDSSD and ZIF-H_2S-SDSSD NP suspensions in PBS (pH = 7.4) to react directly with the BCA working solution. Afterward, the samples were centrifuged at 8000 g for 5 min, and the absorbance of the supernatants was measured. Alternatively, the ZIF-SDSSD and ZIF-H_2S-SDSSD NPs were dissolved in the acidic PBS (pH = 1.0) and reacted with the BCA working solution to assess the total loaded peptide.

The concentration of acid-labile sulfide was determined using the methylene blue (MB) assay, which involved the reaction of sulfide with N, N-dimethyl-p-phenylenediamine sulfate in the presence of the oxidizing agent Fe^{3+}in hydrochloric acid to form MB. Briefly, 75 µl of the NPs suspension were mixed with 250 µl of zinc acetate solution (1 wt% in deionized water), and then MB was formed by adding 150 µl of N, N-dimethyl-p-phenylenediamine sulfate (20 mM in 7.2 M HCl) and 150 µl of $FeCl_3$ (30 mM in 1.2 M HCl). The absorbance at 670 nm was detected after incubation for 15 min, and the concentration of sulfide was determined using a standard curve established by NaHS solution. The NPs suspension with a concentration of 5 mg ml^{-1} reacted directly with the detection solution with strong acidity to evaluate the total loaded sulfide. To study the H_2S-release behavior, the ZIF-H_2S-SDSSD NPs were dispersed in 10 ml of PBS with different pH values (4.7, 5.8, and 7.4) under gentle shaking at 37 °C. At different time points, the NP suspension (75 µl) was collected for the MB assay to determine the remaining sulfide. The pH-responsive release of Zn^{2+} from NP suspension at a concentration of 3 mg ml^{-1} in PBS with different pH values (4.7, 5.8, and 7.4) was investigated. At each time point, the solution was centrifuged, and 3 ml of supernatant was collected, with an equal volume of fresh PBS added to maintain the total volume. The concentration of Zn^{2+} was measured using inductively coupled plasma atomic emission spectrometry (ICP-AES, Optimal 8000, Perkin Elmer, USA). The release of Zn^{2+} was profiled by cumulatively summing the concentrations at each time point. The total antioxidant capacity assay kit (Beyotime, China) was used to evaluate the antioxidant activity of various NPs.

Cytotoxicity Assays: The BMMs and BMSCs were seeded on 96-well plates at a density of 5000 cells/well. After incubation with different concentrations of NPs for 24 h and 72 h, the culture medium was replaced with 100 µl of α-MEM supplemented with 10% CCK-8 reagent (Yeasen, China) and incubated at 37 °C for another 1 h. The absorbance at 450 nm was detected to determine the cell viability. In Live/Dead cell staining, the BMMs and BMSCs were seeded on coverslips in 24-well plates with a density of 50000 cells/well. After incubation with 20 µg ml^{-1} of NPs for 24 and 72 h, the cells were subjected to Live/Dead cell staining (Yeasen, China) and observed under a fluorescence microscope (Zeiss, Germany). Hemolysis assay was carried out to explore the blood compatibility of NPs. Deionized water was set as the positive control and normal saline was set as the negative control. The erythrocytes were incubated with different concentrations of NPs at 37 °C for 1 h. After centrifugation, the absorbance of supernatants at 570 nm were determined.

Intracellular Uptake: The C6-labeled ZIF-H_2S-SDSSD NPs were prepared to assess the intracellular uptake of NPs. The NPs re-dispersed in 5 ml of methanol (2 mg ml^{-1}) were mixed with 1 mg of C6 dissolved in 100 µl of methanol and stirred at room temperature overnight. The product was collected by centrifugation at 800 g for 5 min and washed with methanol to remove loose C6. BMMs and BMSCs were incubated with C6-labeled ZIF-H_2S-SDSSD NPs for different times and stained by LysoTracker (Thermo Fisher, USA) to assess the intracellular delivery of NPs. The stained samples were observed under a fluorescence microscope (Zeiss, Germany).

Macrophage Polarization In Vitro: The BMMs were cultured in complete α-MEM supplemented with the 30 ng ml^{-1} macrophage colony-stimulating factor (M-CSF; R&D, USA), 100 ng ml^{-1} LPS (Sigma-Aldrich, Germany), and 20 ng ml^{-1} IFN-γ (PeproTech, USA) for 24 h to induce macrophage polarization. The various NPs with a concentration of 20 µg ml^{-1} were used to investigate their effect on macrophage reprogramming.

Osteogenic Differentiation In Vitro: The BMSCs were cultured with the osteogenic induction medium, which was complete α-MEM supplemented with 10 mM β-glycerophosphate (Sigma-Aldrich, Germany), 0.25 mM ascorbate (Sigma-Aldrich, Germany), and 0.1µM dexamethasone (Sigma-Aldrich, Germany). The various NPs with a concentration of 20 µg ml^{-1} were utilized to evaluate their effect on the osteogenic differentiation of BMSCs. Prior to the preparation of CM, BMMs were intervened by LPS (100 ng ml^{-1}) and IFN-γ (20 ng ml^{-1}) as well as different NPs (20 µg ml^{-1}). After incubation for 24 h, the supernatant was harvested by centrifugation at 300 g for 5 min, and then mixed with the osteogenic induction medium at a ratio of 1:1. On day 7 after osteogenic induction, ALP staining was conducted with the BCIP/NBT working solution (Beyotime, China), and the ALP-positive area was analyzed by ImageJ software. The ALP activity was investigated using an alkaline phosphatase assay kit (Beyotime, China), and the absorbance was determined at 405 nm. On day 14 after osteogenic induction, ARS staining was performed with the ARS solution (Beyotime, China). The stained calcium crystals were dissolved with hexadecyl pyridinium chloride, and the absorbance was detected at 562 nm.

Osteoclastic Differentiation In Vitro: The BMMs were cultured with osteoclastic induction medium, which was complete α-MEM supplemented with 30 ng ml^{-1} M-CSF (R&D, USA) and 50 ng ml^{-1} receptor activator for nuclear factor-κB ligand (RANKL; R&D Systems, USA). The various NPs with a concentration of 20 µg ml^{-1} were utilized to evaluate their effect on the osteoclastic differentiation of BMMs. Prior to the preparation of CM, BMMs were intervened by LPS (100 ng ml^{-1}) and IFN-γ (20 ng ml^{-1}) as well as different NPs (20 µg ml^{-1}). After incubation for 24 h, the supernatant was collected by centrifugation at 300 g for 5 min, and then mixed with the osteoclastic induction medium at a ratio of 1:1. On day 5 of osteoclastic induction, TRAP staining was conducted using a TRAP staining kit (Amizona Scientific, USA), and the TRAP-positive area was analyzed by ImageJ software.

Immunofluorescence Staining: The BMMs were seeded with a density of 50000 cells/well and the BMSCs were seeded with a density of 30000 cells/well on coverslips using 24-well plates as the holders. The primary antibodies used in immunofluorescence staining included F4/80 (Abcam, UK; ab16911), INOS (ABclonal, China; A3774), CD86 (Proteintech, China; 13395-1-AP), ARG1 (ABclonal, China; A4923), CD206 (Proteintech, China; 18704-1-AP), OCN (ABclonal, China; A6205), HIF-1α (HUABIO, China; HA721997) and IL-1β (ABclonal, China; A16288), and the secondary antibodies used in immunofluorescence staining included Alexa Fluor 594 goat anti-rabbit IgG H&L (ABclonal, China; AS039) and Alexa Fluor 488 goat anti-rat IgG H&L (ABclonal, China; AS019). The cytoskeleton was stained with FITC-labeled phalloidin (ABclonal, China; RM02836) when the nuclei were counterstained with DAPI (Beyotime, China). All the stained samples were observed under a fluorescence microscope (Zeiss, Germany), and the mean fluorescence intensity was analyzed by ImageJ software.

Flow Cytometry: The BMMs were seeded with a density of 600000 cells/well on 6-well plates. After different treatments, the cells were harvested and incubated with the antibodies including F4/80 (Biolegend, USA; 123132), CD86 (Biolegend, USA; 159204), and CD206 (Biolegend, USA; 141706) at room temperature in darkness for 30 min. A mitochondrial membrane potential assay kit with JC-1 (Beyotime, China) was used to detect $\Delta\psi$m, and a mitochondrial superoxide assay kit with MitoSOX red (Beyotime, China) was employed to detect mitochondrial superoxide. All the stained cells were analyzed by flow cytometry (Thermo Fisher, USA) and FlowJo software.

ELISA: The BMMs were intervened by LPS (100 ng ml^{-1}) and IFN-γ (20 ng ml^{-1}) as well as different NPs (20 µg ml^{-1}). After incubation for 24 h, the supernatant was harvested by centrifugation at 300 g for 5 min. The IL-1β ELISA kit (ABclonal, China; RK00006) and IL-10 ELISA kit (ABclonal, China; RK00016) were used to detect the level of IL-1β and IL-10 in the supernatant.

RT-qPCR Assay: The total RNA was extracted using the Trizol reagent (Beyotime, China), and the reverse transcription reaction was conducted with the HiScript III RT SuperMix (Vazyme, China). Gene expression analysis was carried out with the qPCR SYBR Green Master Mix (Vazyme, China) using a CFX96 Real-time PCR Detection System (Bio-Rad, USA). The sequences of primers are shown in Table S4, Supporting Information.

Transcriptome Sequencing and Metabolomic Analysis: After LPS/IFN-γ stimulation, the BMMs were collected from the ZIF-H_2S-SDSSD group and control group. Transcriptome sequencing and metabolomic LC-MS were conducted by OE Biotech Co (China). Thresholds for statistically differential expression were set as q values <0.05 and |log2foldchange|>1. GO enrichment analysis, KEGG enrichment analysis, and GSEA were performed among DEGs.

Seahorse Extracellular Flux Analysis: The BMMs were seeded on Seahorse XFe24 cell culture plates (Agilent, USA) with a density of 300000 cells/well. After incubation with LPS/IFN-γ or LPS/IFN-γ+ZIF-H_2S-SDSSD NPs, the intervention medium was replaced with the fresh medium and then incubated in a humidified CO_2-free incubator for 1 h. The probe plates were hydrated overnight in a humidified CO_2-free incubator before analysis. For the glycolytic stress assay, glucose (10 mM), oligomycin (oligo, 1.5 μM), and 2-deoxy-D-glucose (2-DG, 50 mM) were sequentially injected into cell culture plates. For the mitochondrial stress assay, oligo (1.5 μM), carbonyl cyanide p-trifluoromethoxyphenylhydrazone (FCCP, 1 μM), and rotenone/antimycin A (R/A, 0.5 μM) were sequentially injected into cell culture plates. The ECAR and OCR of macrophages were determined with a Seahorse XFe24 analyzer (Agilent, USA).

Establishment of Osteoporotic Fracture and Experimental Intervention: The Animal Ethics Committee of Soochow University authorized the animal experiments (approval number: SUDA20240308A01). Postmenopausal osteoporosis was induced in 8-week-old C57BL/6 mice by OVX under anesthesia (100 mg kg^{-1} ketamine and 10 mg kg^{-1} xylazine, intraperitoneal injection). After four weeks, a transverse fracture of the left middle femur was made and fixed with a 26 g needle inserted into the medullary cavity. From 48 h after fracture surgery, different NPs with a concentration of 5 mg kg^{-1} and normal saline were administered intravenously every three days. Similarly, the normal fracture was made on mice without osteoporosis and ZIF-H_2S-SDSSD NPs or normal saline were administered intravenously.

In Vivo Biodistribution: The Cy7-labeled ZIF-H_2S NPs and ZIF-H_2S-SDSSD NPs were prepared to assess the in vivo biodistribution of NPs. The NPs re-dispersed in 5 ml of methanol (2 mg ml^{-1}) were mixed with 1 mg of Cy7 dissolved in 100 μl of methanol and stirred at room temperature overnight. The product was collected by centrifugation at 800 g for 5 min and washed with methanol to remove loose Cy7. Each mouse was injected intravenously with 0.1 mL (1 mg mL^{-1}) Cy7-labeled ZIF-H_2S NPs or ZIF-H_2S-SDSSD NPs. At 12 h and 24 h after NPs injection, the mice or the collected major organs (heart, liver, spleen, lung, kidney, and femur) were imaged by the Lumina III In Vivo Imaging System (PerkinElmer, USA).

Radiological Analysis: The Skyscan1176 micro-CT system (Bruker, Germany) was used to analyze the femurs on the 7^{th}, 14^{th} and 28^{th} day after fracture surgery. The scanning parameters were set as follows: voltage = 50 kV, current = 200 μA, and layer thickness = 9 μm. After scanning, the images were 3D-reconstructed, and the morphometric parameters, including BV/TV, BS/TV, Tb.N, Tb.Sp, and callus index, were measured.

Histological Staining: The femurs were fixed with 10% neutral buffered formalin for 48 h and decalcified with the ethylenediaminetetraacetic acid (EDTA) solution for 1 month. Osteoporosis and fracture healing were assessed by H&E staining and Masson staining, and the osteoclastic levels were investigated by Trap staining. Immunofluorescence staining and immunohistochemical staining were carried out to evaluate the macrophage polarization and cytokine secretion. The primary antibodies used in histological staining included F4/80 (Abcam, ab16911), CD86 (Proteintech, 13395-1-AP), CD206 (Proteintech, 18704-1-AP), POSTN (Proteintech, 19899-1-AP), IL-1β (ABclonal, A16288) and IL-10 (ABclonal, A2171). The histological sections were observed under a microscope and analyzed by ImageJ software.

Statistical Analysis: The data were presented as mean ± standard deviation. The unpaired student's t-test was performed to verify the significance of differences between two groups, and one-way ANOVA with Tukey's test was conducted for multiple comparisons. The statistical analysis was performed with the GraphPad Prism 8.0 software, and the statistical significance was defined as $p < 0.05$.

Supporting Information

Supporting Information is available from the Wiley Online Library or from the author.

Acknowledgements

Y.Q., Z.Z., and X.G. contributed equally to this work. The schematic illustrations in this work were partially drawn using www.biorender.com. This work was supported by the National Natural Science Foundation of China (82072425, 82072498, 82272567, 82350710800), the Natural Science Foundation of Jiangsu Province (BK2021650), the China Postdoctoral Science Foundation (No.:2017T100320), the Shenzhen Science and Technology Program (JCYJ20210324101800002), the Guangdong Basic and Applied Basic Research Foundation (2022A1515010528, 2024A1515012397), Priority Academic Program Development of Jiangsu Higher Education Institutions (PAPD), Jiangsu Medical Research Project (ZD2022014), the Program of Suzhou Health Commission (GSWS2022002), the Tianshan Talent Training Program of Xinjiang Uygur Autonomous Region: Youth Support Talent Project (2023TSYCQNTJ0018), the National and Local Engineering Laboratory of New Functional Polymer Materials (SDGC2205), the Postgraduate Research & Practice Innovation Program of Jiangsu Province (KYCX22_3217), as well as City University of Hong Kong Donation Research Grants (Nos. DON-RMG 9229021 and 9229021).

Conflict of Interest

The authors declare no conflict of interest.

Data Availability Statement

The data that support the findings of this study are available in the supplementary material of this article.

Keywords

bone targeting, hydrogen sulfide, macrophage polarization, metabolic reprogramming, osteoporotic fracture

Received: October 7, 2024
Revised: December 6, 2024
Published online: December 23, 2024

[1] M. D. Walker, E. Shane, *N. Engl. J. Med.* **2023**, *389*, 1979.
[2] K. Rapp, S. E. Lamb, P. Roigk, C. Becker, C. Konnopka, H.-H. König, R. S. Peter, D. Rothenbacher, G. Büchele, *BMC Med.* **2022**, *20*, 49.
[3] a) T. Chattaris, G. Oh, N. A. Gouskova, D. H. Kim, D. P. Kiel, S. D. Berry, *J. Bone Miner. Res.* **2022**, *37*, 2103; b) I. R. Reid, *Nat. Rev. Endocrinol.* **2020**, *16*, 333.
[4] S. E. Sattui, K. G. Saag, *Nat. Rev. Endocrinol.* **2014**, *10*, 592.
[5] C.-W. Sing, T.-C. Lin, S. Bartholomew, J. S. Bell, C. Bennett, K. Beyene, P. Bosco-Levy, B. D. Bradbury, A. H. Y. Chan, M. Chandran, C. Cooper, M. de Ridder, C. Y. Doyon, C. Droz-Perroteau, G. Ganesan, S. Hartikainen, J. Ilomaki, H. E. Jeong, D. P. Kiel, K. Kubota, E. C.-C. Lai, J. L. Lange, E. M. Lewiecki, J. Lin, J. Liu, J. Maskell, M. M. de Abreu, J. O'Kelly, N. Ooba, A. B. Pedersen, et al., *J. Bone Miner. Res.* **2023**, *38*, 1064.
[6] C. Ayers, D. Kansagara, B. Lazur, R. Fu, A. Kwon, C. Harrod, *Ann. Intern. Med.* **2023**, *176*, 182.

[7] V. Hegde, J. E. Jo, P. Andreopoulou, J. M. Lane, *Osteoporos. Int.* **2016**, *27*, 861.
[8] a) L. Claes, S. Recknagel, A. Ignatius, *Nat. Rev. Rheumatol.* **2012**, *8*, 133; b) X. Chen, X. Li, W. He, M. Wang, A. Gao, L. Tong, S. Guo, H. Wang, G. Pan, *The Innovation.* **2023**, *4*, 100483.
[9] D. Saul, S. Khosla, *Endocr. Rev.* **2022**, *43*, 984.
[10] a) J. Li, X. Jiang, H. Li, M. Gelinsky, Z. Gu, *Adv. Mater.* **2021**, *33*, 2004172; b) C. Schlundt, H. Fischer, C. H. Bucher, C. Rendenbach, G. N. Duda, K. Schmidt-Bleek, *Acta Biomater.* **2021**, *133*, 46; c) Y. Wu, H. Wang, P. K. Chu, *The Innovation Life.* **2023**, *1*, 100027.
[11] J. Van den Bossche, L. A. O'Neill, D. Menon, *Trends Immunol.* **2017**, *38*, 395.
[12] a) J. Xue, S. V. Schmidt, J. Sander, A. Draffehn, W. Krebs, I. Quester, D. De Nardo, T. D. Gohel, M. Emde, L. Schmidleithner, H. Ganesan, A. Nino-Castro, M. R. Mallmann, L. Labzin, H. Theis, M. Kraut, M. Beyer, E. Latz, T. C. Freeman, T. Ulas, J. L. Schultze, *Immunity.* **2014**, *40*, 274; b) L. Tong, A. J. V. Wijnen, H. Wang, D. Chen, *The Innovat. Life.* **2024**, *2*, 100078; c) Z. Du, F. Qiao, L. Tong, W. Zhang, X. Mou, X. Zhao, M. F. Maitz, H. Wang, N. Huang, Z. Yang, *The Innovation.* **2024**, *5*, 100671.
[13] a) Y. Xu, Y. Li, A. Gao, P. K. Chu, H. Wang, *The Innovat. Life.* **2023**, *1*, 100015; b) S.-E. Byun, K.-J. Lee, W. C. Shin, N. H. Moon, C.-H. Kim, *Osteoporos. Int.* **2023**, *34*, 1323; c) X. Gao, L. Yan, W. Zhang, Y. Lv, P. Ou, R. Hang, A. Gao, L. Tong, P. K. Chu, H. Wang, *Nano Today.* **2023**, *53*, 102047.
[14] M. Jiang, T. Wang, X. Yan, Z. Liu, Y. Yan, K. Yang, J. Qi, H. Zhou, N. Qian, Q. Zhou, B. Chen, X. Xu, X. Xi, C. Yang, L. Deng, *J. Bone Miner. Res.* **2019**, *34*, 361.
[15] a) G. Cirino, C. Szabo, A. Papapetropoulos, *Physiol. Rev.* **2023**, *103*, 31; b) N. Dilek, A. Papapetropoulos, T. Toliver-Kinsky, C. Szabo, *Pharmacol. Res.* **2020**, *161*, 105119.
[16] a) Y. Hao, H. Wang, L. Fang, J. Bian, Y. Gao, C. Li, *Front. Pharmacol.* **2021**, *12*, 661601; b) T. Yue, J. Li, J. Zhu, S. Zuo, X. Wang, Y. Liu, J. Liu, X. Liu, P. Wang, S. Chen, *Cancer Res.* **2023**, *83*, 595.
[17] R. Ettlinger, U. Lächelt, R. Gref, P. Horcajada, T. Lammers, C. Serre, P. Couvreur, R. E. Morris, S. Wuttke, *Chem. Soc. Rev.* **2022**, *51*, 464.
[18] a) L. Chen, D. Wang, J. Qiu, X. Zhang, X. Liu, Y. Qiao, X. Liu, *Bioact. Mater.* **2021**, *6*, 191; b) S. Liu, Z. Lin, W. Qiao, B. Chen, J. Shen, *Eng. Regener.* **2024**, *5*, 375; c) F. L. Zhao, A. Gao, Q. Liao, Y. Y. Li, I. Ullah, Y. Zhao, X. X. Ren, L. P. Tong, X. Li, Y. D. Zheng, P. K. Chu, H. Y. Wang, *Adv. Funct. Mater.* **2024**, *34*, 2310726.
[19] a) A. T. Stoltzfus, J. G. Ballot, T. Vignane, H. Li, M. M. Worth, L. Muller, M. A. Siegler, M. A. Kane, M. R. Filipovic, D. P. Goldberg, S. L. J. Michel, *Angew. Chem., Int. Ed.* **2024**, *63*, 202401003; b) N. Yoshinari, N. Kuwamura, T. Kojima, T. Konno, *Coord. Chem. Rev.* **2023**, *474*, 214857.
[20] K. Hu, Z. Shang, X. Yang, Y. Zhang, L. Cao, *J. Inflamm. Res.* **2023**, *16*, 3563.
[21] D.-D. Wu, S. Jin, R.-X. Cheng, W.-J. Cai, W.-L. Xue, Q.-Q. Zhang, L.-J. Yang, Q. Zhu, M.-Y. Li, G. Lin, Y.-Z. Wang, X.-P. Mu, Y. Wang, I. Y. Zhang, Q. Zhang, Y. Chen, S.-Y. Cai, B. Tan, Y. Li, Y.-Q. Chen, P.-J. Zhang, C. Sun, Y. Yin, M.-J. Wang, Y.-Z. Zhu, B.-B. Tao, J.-H. Zhou, W.-X. Huang, Y.-C. Zhu, *Cell Rep.* **2023**, *42*, 112750.
[22] J. Dong, W. Zhou, X. Hu, J. Bai, S. Zhang, X. Zhang, L. Yu, P. Yang, L. Kong, M. Liu, X. Shang, Z. Su, D. Geng, C. Zhu, *Biomaterials.* **2024**, *307*, 122515.
[23] J. Mosquera, I. García, L. M. Liz-Marzán, *Acc. Chem. Res.* **2018**, *51*, 2305.
[24] G. Ge, W. Wang, Q. Wang, M. Wang, T. Wang, L. Yu, X. Zhang, C. Zhu, Y. Xu, H. Yang, J. Bai, G. Pan, D. Geng, *Adv. Funct. Mater.* **2024**, *34*, 2315849.
[25] E. Mills, L. A. J. O'Neill, *Trends Cell. Biol.* **2014**, *24*, 313.
[26] W. K. E. Ip, N. Hoshi, D. S. Shouval, S. Snapper, R. Medzhitov, *Science.* **2017**, *356*, 513.
[27] S. Liu, S. Liu, B. He, L. Li, L. Li, J. Wang, T. Cai, S. Chen, H. Jiang, *EMBO Rep.* **2021**, *22*, e51606.
[28] S. E. Weinberg, L. A. Sena, N. S. Chandel, *Immunity.* **2015**, *42*, 406.
[29] a) S. E. Corcoran, L. A. J. O'Neill, *J. Clin. Invest.* **2016**, *126*, 3699; b) G. M. Tannahill, A. M. Curtis, J. Adamik, E. M. Palsson-McDermott, A. F. McGettrick, G. Goel, C. Frezza, N. J. Bernard, B. Kelly, N. H. Foley, L. Zheng, A. Gardet, Z. Tong, S. S. Jany, S. C. Corr, M. Haneklaus, B. E. Caffrey, K. Pierce, S. Walmsley, F. C. Beasley, E. Cummins, V. Nizet, M. Whyte, C. T. Taylor, H. Lin, S. L. Masters, E. Gottlieb, V. P. Kelly, C. Clish, P. E. Auron, et al., *Nature.* **2013**, *496*, 238.
[30] a) E. T. Chouchani, V. R. Pell, E. Gaude, D. Aksentijević, S. Y. Sundier, E. L. Robb, A. Logan, S. M. Nadtochiy, E. N. J. Ord, A. C. Smith, F. Eyassu, R. Shirley, C.-H. Hu, A. J. Dare, A. M. James, S. Rogatti, R. C. Hartley, S. Eaton, A. S. H. Costa, P. S. Brookes, S. M. Davidson, M. R. Duchen, K. Saeb-Parsy, M. J. Shattock, A. J. Robinson, L. M. Work, C. Frezza, T. Krieg, M. P. Murphy, *Nature.* **2014**, *515*, 431; b) C. T. Taylor, C. C. Scholz, *Nat. Rev. Nephrol.* **2022**, *18*, 573.
[31] K. Zheng, J. Bai, W. Chen, Y. Xu, H. Yang, W. Li, P. Li, L. Tong, H. Wang, P. K. Chu, D. Geng, *Adv. Funct. Mater.* **2023**, *33*, 2214126.
[32] a) G. Jin, H. Qin, H. Cao, S. Qian, Y. Zhao, X. Peng, X. Zhang, X. Liu, P. K. Chu, *Biomaterials.* **2014**, *35*, 7699; b) Y. Liu, R. Yang, X. Liu, Y. Zhou, C. Qu, T. Kikuiri, S. Wang, E. Zandi, J. Du, I. S. Ambudkar, S. Shi, *Cell Stem Cell.* **2014**, *15*, 66.
[33] a) H. S. Gong, C. H. Song, Y. H. Lee, S. H. Rhee, H. J. Lee, G. H. Baek, *J. Bone Joint Surg. Am.* **2012**, *94*, 1729; b) W. C. Shin, N. H. Moon, J. H. Jang, H. U. Seo, K. T. Suh, *Bone.* **2019**, *128*, 115033.
[34] Y. Sun, X. Ye, M. Cai, X. Liu, J. Xiao, C. Zhang, Y. Wang, L. Yang, J. Liu, S. Li, C. Kang, B. Zhang, Q. Zhang, Z. Wang, A. Hong, X. Wang, *ACS Nano.* **2016**, *10*, 5759.

Supporting Information for

A Bone-Targeting Hydrogen Sulfide Delivery System for Treatment of Osteoporotic Fracture via Macrophage Reprogramming and Osteoblast-Osteoclast Coupling

Yi Qin,[1]† Zhen Zhang,[2]† Xiaobin Guo,[6]† Wenhao Li,[1] Wenyu Xia,[1] Gaoran Ge,[1] Yanyue Li,[2] Min Guan,[2] Ang Gao,[2]* Lu Mao,[5]* Huaiyu Wang,[2,4]* Paul K. Chu,[3] Dechun Geng [1]*

[1] Department of Orthopedics, The First Affiliated Hospital of Soochow University, Orthopedic Institute, Medical College, Soochow University, Suzhou, 215006, Jiangsu, China.

[2] Center for Human Tissues and Organs Degeneration, Shenzhen Institute of Advanced Technology, Chinese Academy of Sciences, Shenzhen, 518055, China

[3] Department of Physics, Department of Materials Science and Engineering, and Department of Biomedical Engineering, City University of Hong Kong, Tat Chee Avenue, Kowloon, Hong Kong, 999077, China

[4] The Key Laboratory of Biomedical Imaging Science and System, Chinese Academy of Sciences, Shenzhen, 518055, China

[5] Department of Spine Surgery, Zhongda Hospital, Southeast University, Nanjing, 210009, Jiangsu, China

[6] Department of Orthopedics, First Affiliated Hospital of Xinjiang Medical University, Urumqi, 830054, Xinjiang, China

*Corresponding authors. Email: ang.gao1@siat.ac.cn (A. G.); bobai0008@163.com (L. M.); hy.wang1@siat.ac.cn (H. W.); szgengdc@suda.edu.cn (D. G.)

†These authors contributed equally to this work.

The file includes:

Figures S1 to S19

Tables S1 to S4

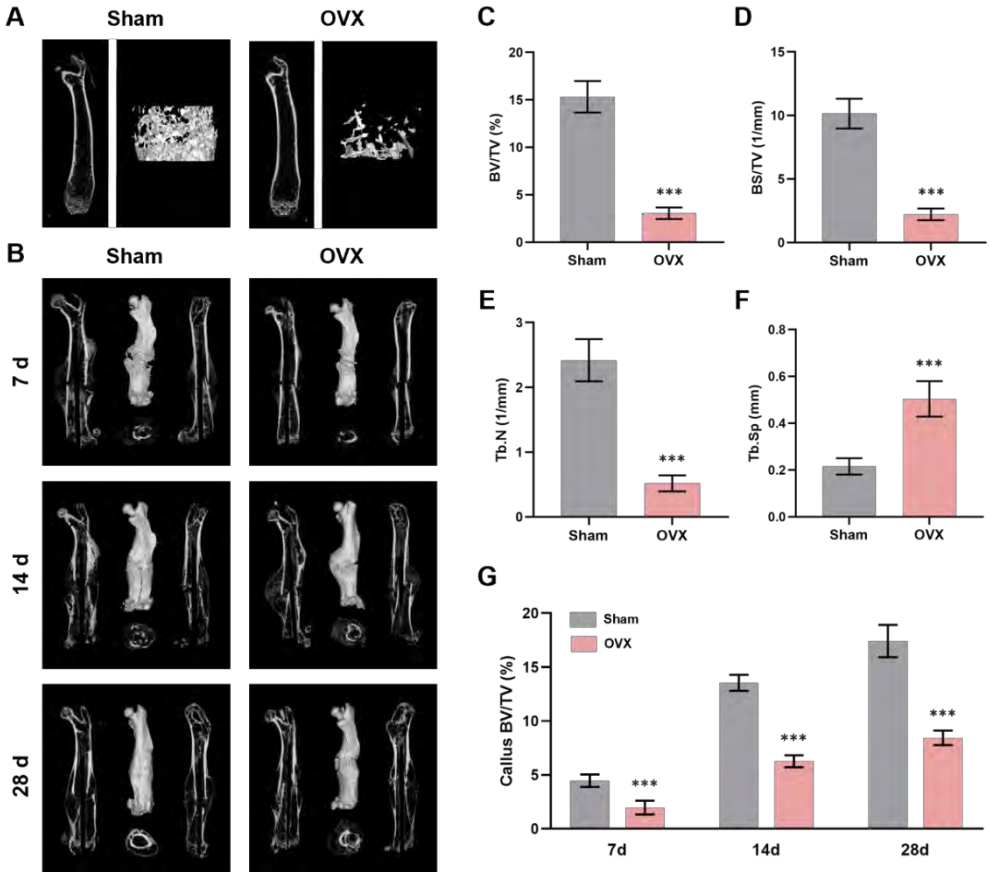

Figure S1. Bone morphological analysis of normal mice and OVX-induced mice. A) Representative images of micro-CT and 3D reconstruction of distal femur trabecular. B) Representative images of micro-CT and 3D reconstruction of femur fracture. C-F) Micro-CT measurements of BV/TV, BS/TV, Tb.N, and Tb.Sp of trabeculae under the distal femur growth plate (n = 5 per group). G) Micro-CT measurements of callus BV/TV at different time points after fracture surgery (n = 5 per group). The data are presented as the mean ± SD. Statistical analysis is performed by the unpaired Student's t-test. Compared with the sham group, ***$p < 0.001$.

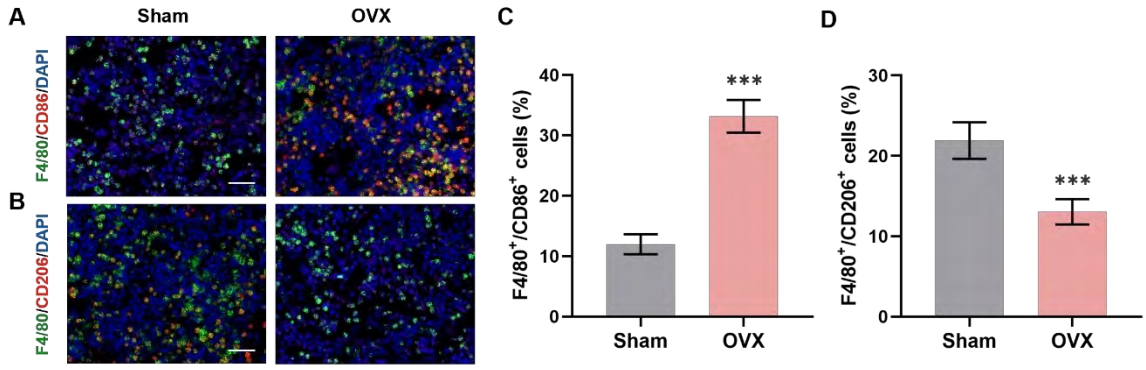

Figure S2. Immunofluorescence staining and quantitative evaluation of fracture callus on 7 days post-surgery (green: F4/80, red: M1 macrophages markers CD86 and M2 macrophages markers CD206, blue: DAPI, scale bar = 100 μm, n = 5 per group). The data are presented as mean ± SD. Statistical analysis is performed by the unpaired Student's t-test. Compared with the sham group, ***$p < 0.001$.

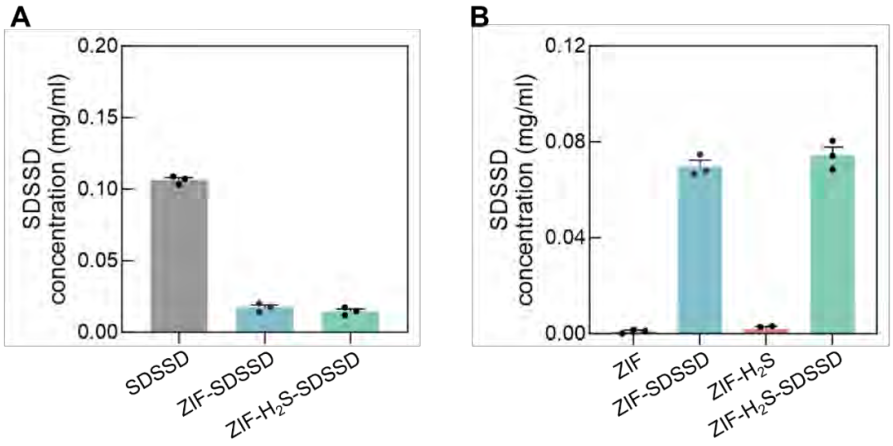

Figure S3. BCA protein assay of the grafting of SDSSD peptide. A) Detection of supernatant after the mixture of SDSSD peptides with ZIF and ZIF-H_2S (n = 3 per group). B) Detection of ZIF NPs, ZIF-SDSSD NPs, ZIF-H_2S NPs, and ZIF-H_2S-SDSSD NPs dissolved in an acidic solution with a pH of 1.0 (n = 3 per group).

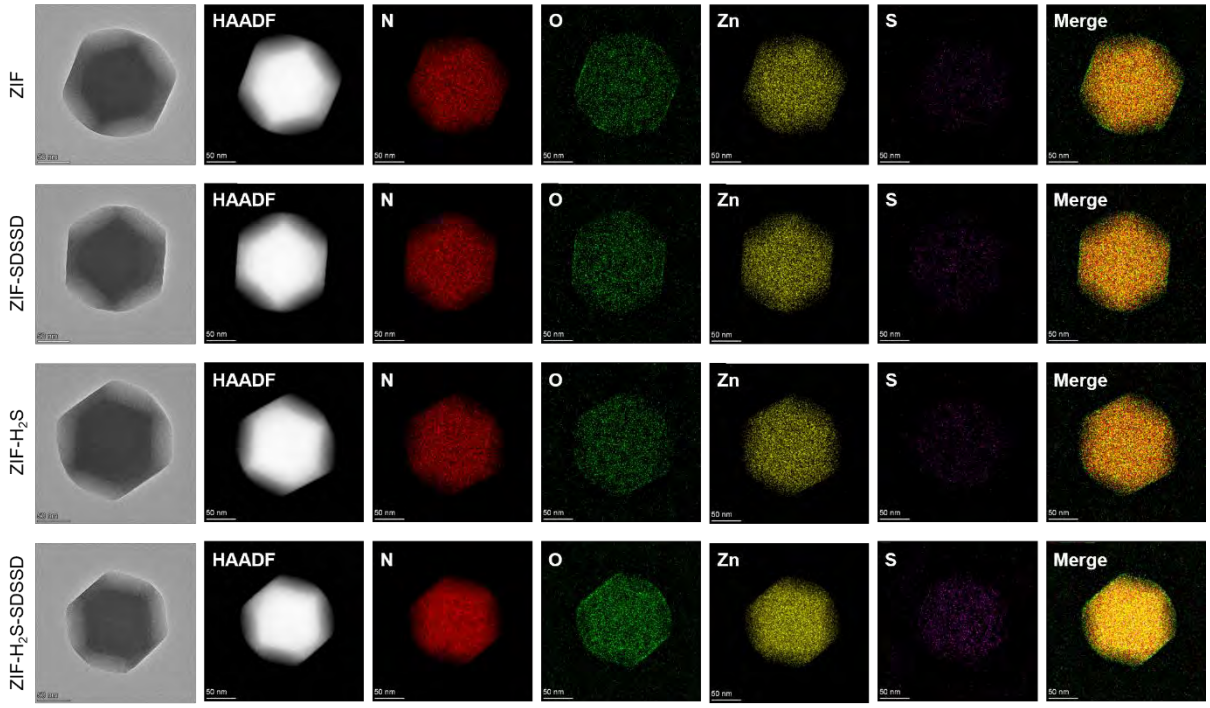

Figure S4. Elemental maps (N, O, Zn, and S) of different NPs by EDS.

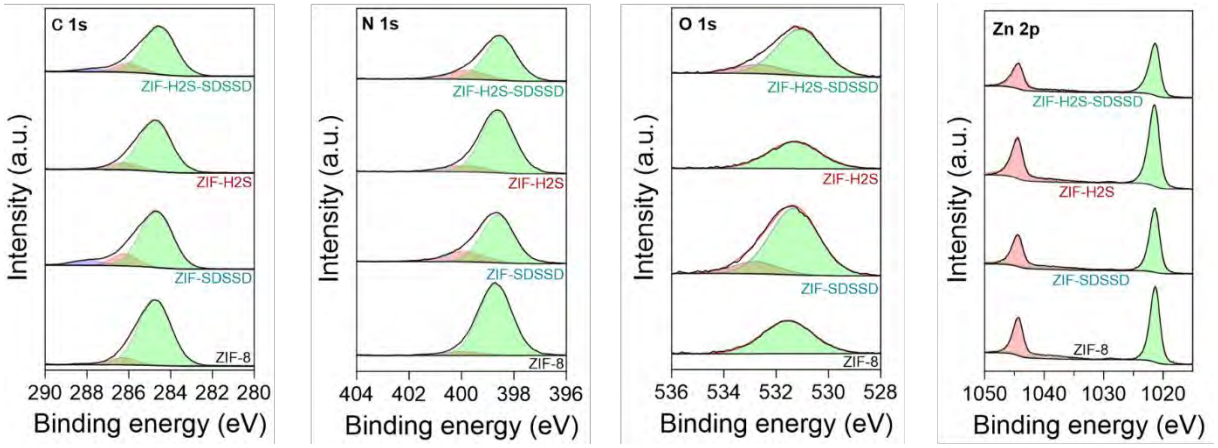

Figure S5. High-resolution C 1s, N 1s, O 1s, and Zn 2p XPS spectra of different NPs.

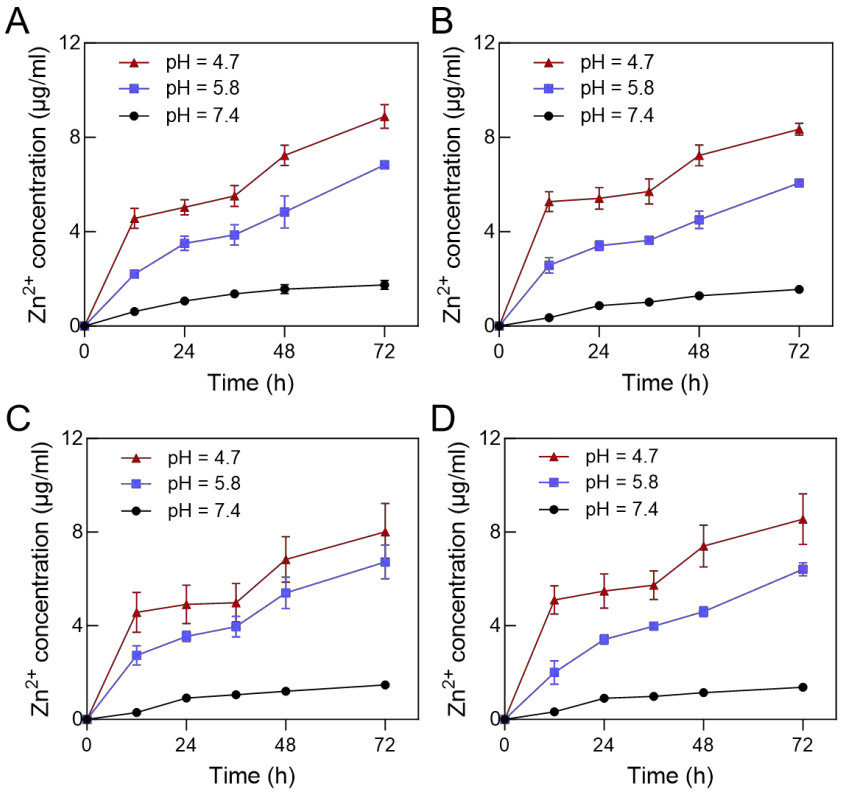

Figure S6. Cumulative release profiles of Zn^{2+} from 3 mg/ml NPs under different pH conditions. A) ZIF NPs, B) ZIF-SDSSD NPs, C) ZIF-H_2S NPs, and D) ZIF-H_2S-SDSSD NPs.

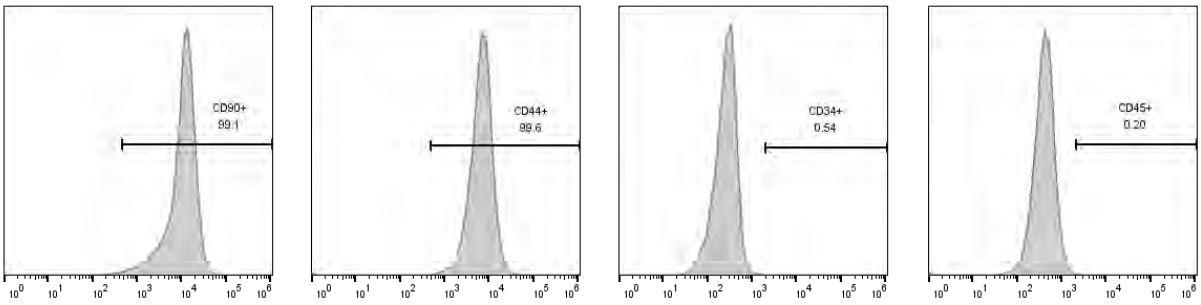

Figure S7. Surface markers of isolated BMSCs identified by flow cytometry, showing a profile of $CD90^+/CD44^+/CD34^-/CD45^-$.

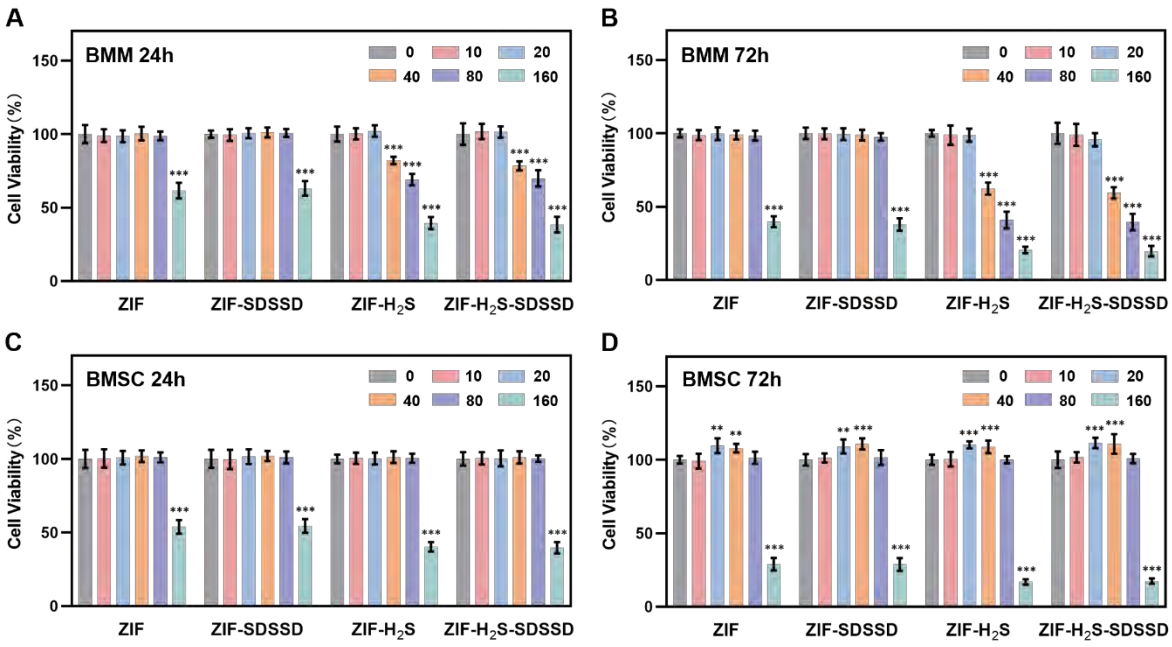

Figure S8. CCK-8 assay of BMMs and BMSCs incubated with different NPs at various concentrations for 24 h and 72 h (n = 6 per group). The data are presented as the mean ± SD. Statistical analysis is performed by one-way ANOVA with Tukey's test. Compared with the 0 μg/ml group, $^{**}p < 0.01$, $^{***}p < 0.001$.

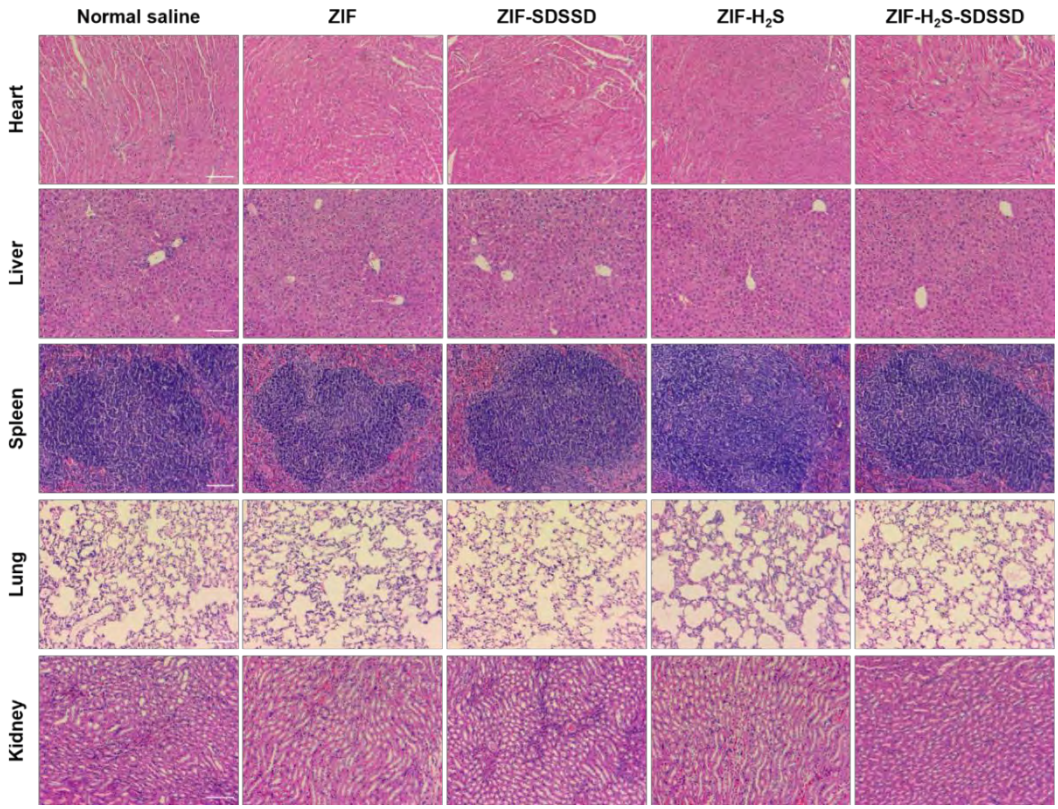

Figure S9. H&E staining of heart, liver, spleen, lung and kidney from C57BL/6 mice receiving intravenous injection of normal saline, ZIF NPs, ZIF-SDSSD NPs, ZIF-H_2S NPs, and ZIF-H_2S-SDSSD NPs for three months (scale bar = 200 μm).

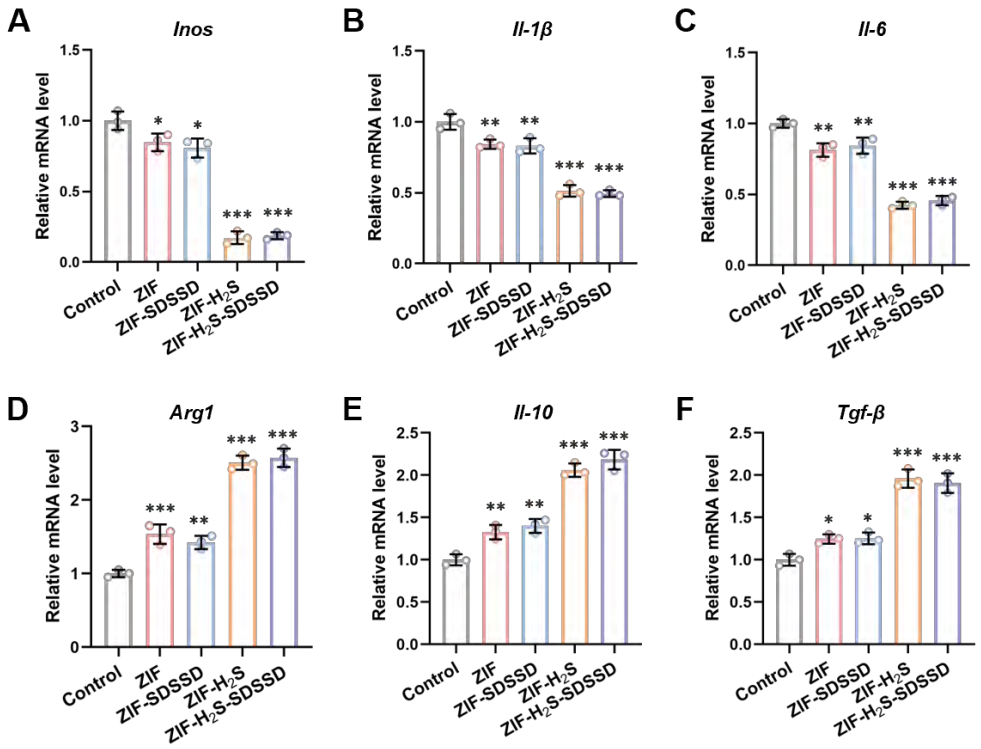

Figure S10. RT-qPCR analysis of BMMs in different groups. A-C) Gene expression levels of pro-inflammatory genes (n=3 per group). D-F) Gene expression levels of anti-inflammatory genes (n=3 per group). The data are presented as the mean ± SD. Statistical analysis is performed by one-way ANOVA with Tukey's test. Compared with the control group, *$p < 0.05$, **$p < 0.01$, ***p < 0.001.

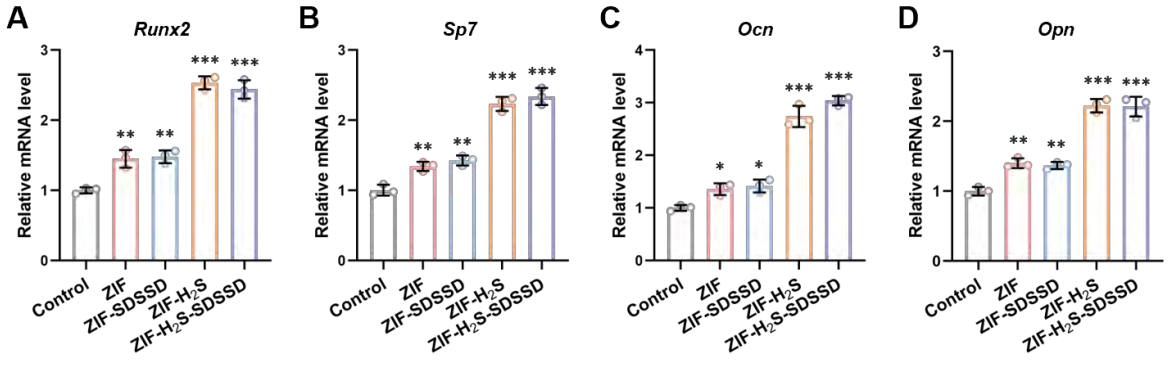

Figure S11. RT-qPCR analysis of BMSCs cultured with CM in different groups. A-D) Gene expression levels of osteogenesis-related genes (n=3 per group). The data are presented as the

mean ± SD. Statistical analysis is performed by one-way ANOVA with Tukey's test. Compared with the control group, *$p < 0.05$, **$p < 0.01$, ***$p < 0.001$.

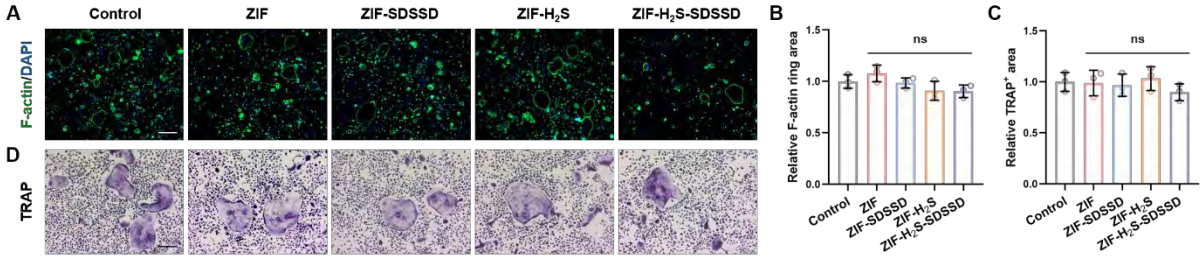

Figure S12. F-actin ring staining and TRAP staining of osteoclasts incubated with CM from BMMs. A, B) F-actin ring staining images and quantitative evaluation of osteoclasts (green: F-actin, blue: DAPI, scale bar = 200 μm, n = 3 per group). C, D) TRAP staining images and quantitative evaluation (scale bar = 100 μm, n = 3 per group). The data are presented as the mean ± SD. Statistical analysis is performed by one-way ANOVA with Tukey's test. Compared with the control group, ns indicates no significant difference.

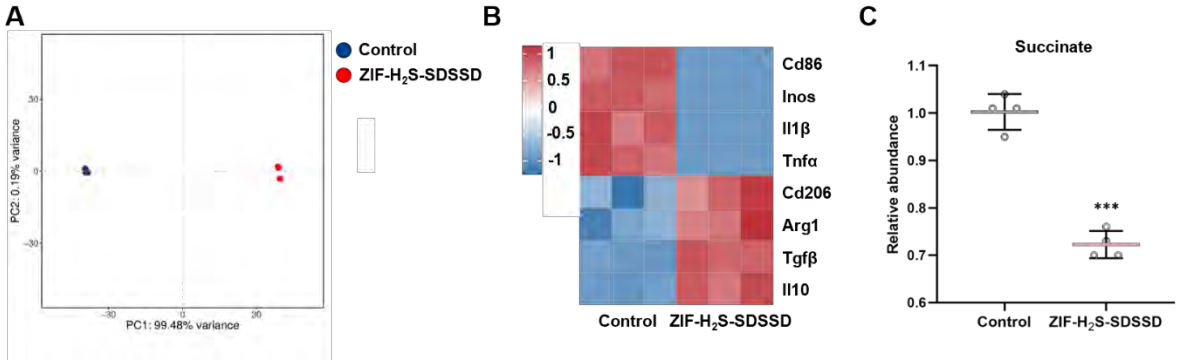

Figure S13. Transcriptome sequencing and metabolomic analysis of the LPS/IFN-γ stimulated BMMs with or without ZIF-H_2S-SDSSD intervention. A) Principal component analysis (PCA) (n=3 per group). B) Heat map of genes associated with macrophage polarization (n = 3 per group). C) Relative abundance of succinate detected by LC-MS (n = 4 per group). Statistical analysis is performed by the unpaired Student's t-test. Compared with the control group, ***p < 0.001.

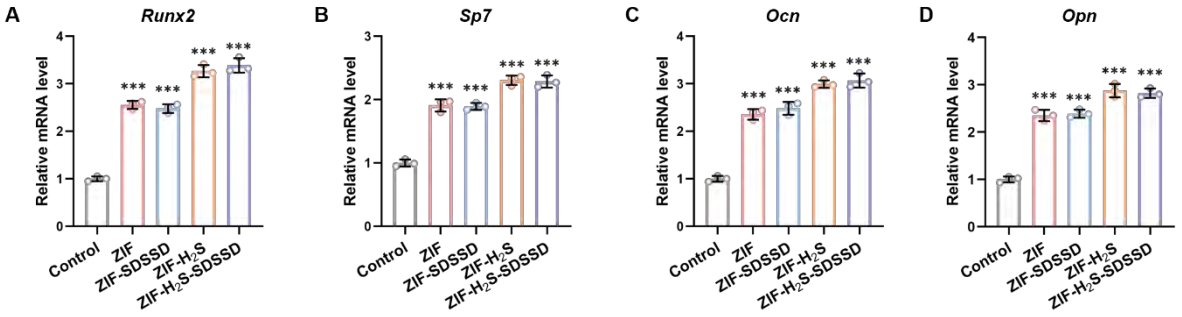

Figure S14. RT-qPCR analysis of BMSCs in different groups. A-D) Gene expression levels of osteogenesis-related genes (n = 3 per group). The data are presented as the mean ± SD. Statistical analysis is performed by one-way ANOVA with Tukey's test. Compared with the control group, ***$p < 0.001$.

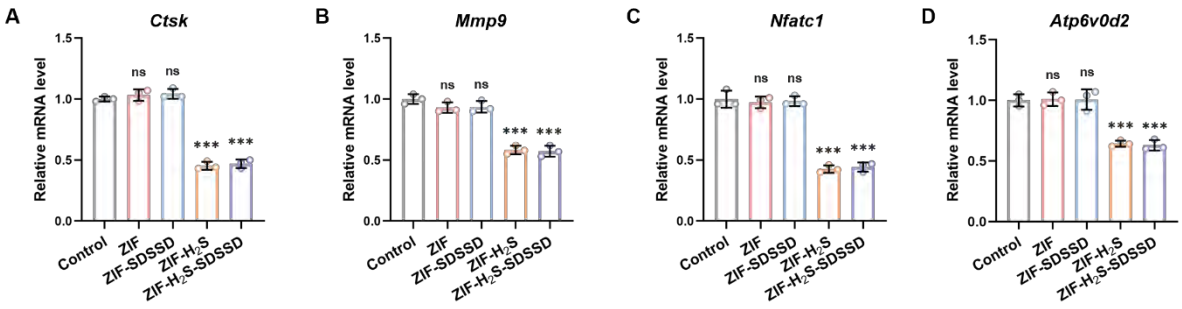

Figure S15. RT-qPCR analysis of osteoclasts in different groups. A-D) Gene expression levels of osteoclastogenesis-related genes (n = 3 per group). The data are presented as the mean ± SD. Statistical analysis is performed by one-way ANOVA with Tukey's test. Compared with the control group, ns indicates no significant difference, ***$p < 0.001$

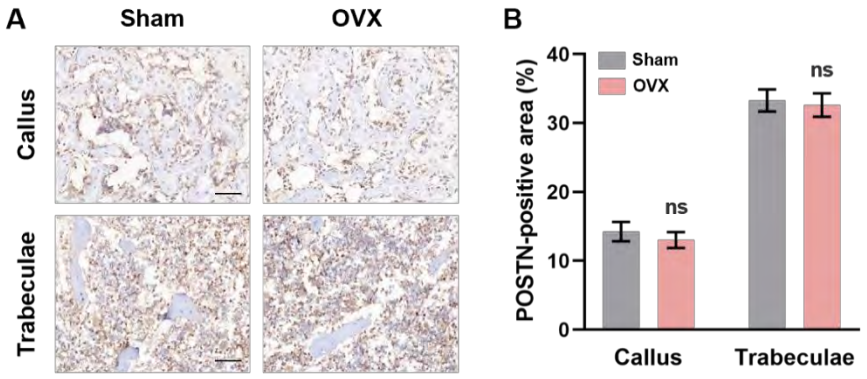

Figure S16. Immunohistochemical staining and quantitative evaluation of POSTN in callus and trabeculae regions (scale bar = 100 μm, n = 5 per group). Compared with the sham group, ns indicates no significant difference.

.

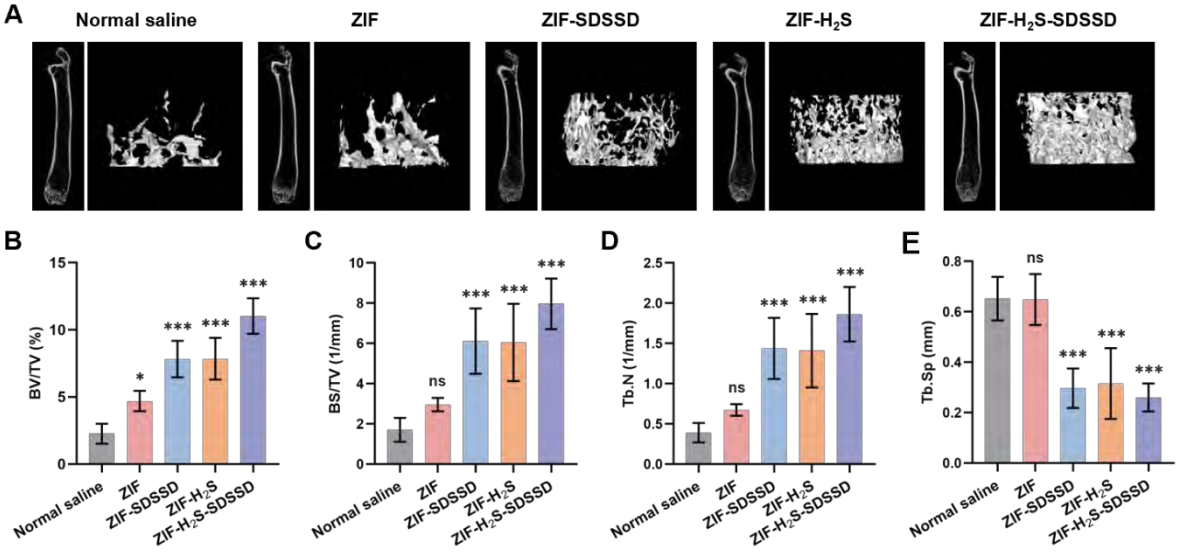

Figure S17. Therapeutic effects on osteoporosis *in vivo*. A) Representative images of micro-CT and 3D reconstruction of osteoporosis after different treatments. B-E) Micro-CT measurements of BV/TV, BS/TV, Tb.N and Tb.Sp of trabeculae under the distal femur growth plate 28 days after fracture surgery (n = 5 per group). The data are presented as the mean ± SD. Statistical analysis is performed by one-way ANOVA with Tukey's test. Compared with the control group, ns indicates no significant difference, $*p < 0.05$, $***p < 0.001$.

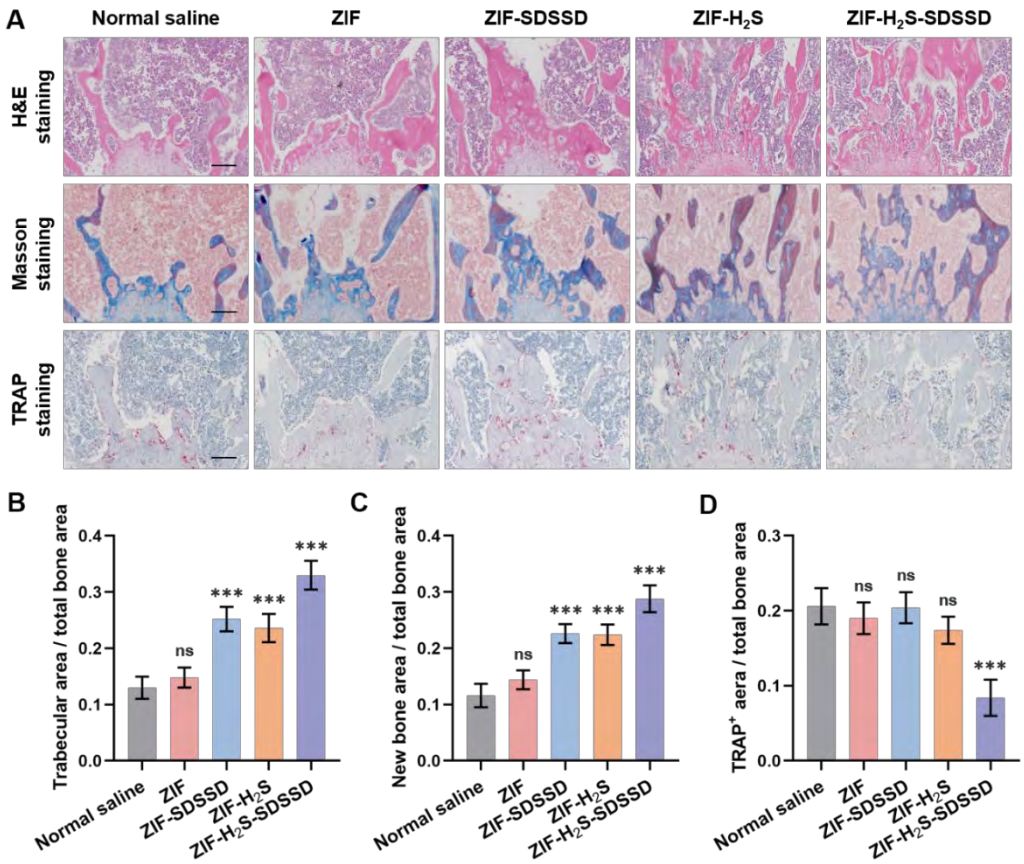

Figure S18. Histological staining of trabeculae under the distal femur growth plate on day 28 post-surgery and quantitative evaluation (scale bar = 100 μm, n = 5 per group). The data are presented as the mean ± SD. Statistical analysis is performed by one-way ANOVA with Tukey's test. Compared with the normal saline group, ns indicates no significant difference, *$p < 0.05$, **$p < 0.01$, ***$p < 0.001$.

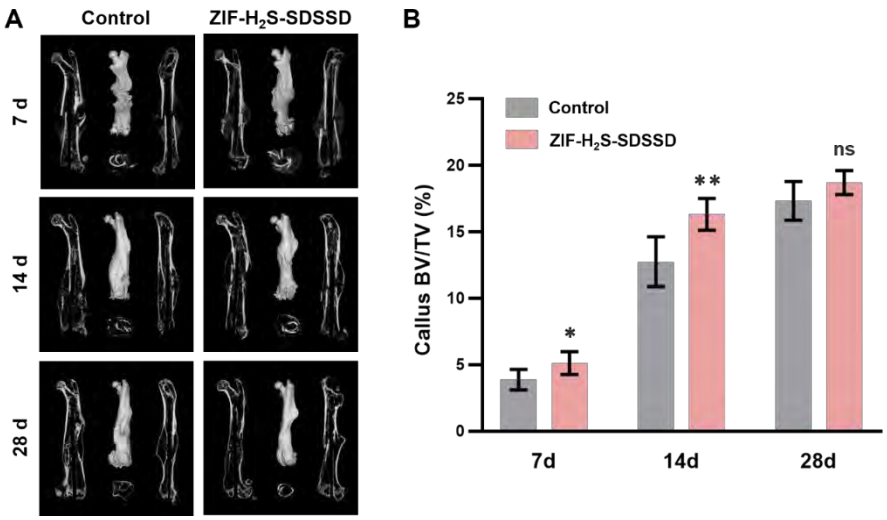

Figure S19. ZIF-H_2S-SDSSD NPs promote normal fracture healing. A) Representative images of micro-CT and 3D reconstruction of femur fracture. B) Micro-CT measurements of callus BV/TV at different time point after fracture surgery (n = 5 per group). The data are presented as the mean ± SD. Statistical analysis is performed by unpaired Student's t-test. Compared with control group, ns indicates no significant difference, *$p < 0.05$, **$p < 0.01$.

Table S1. Elemental concentrations (N, O, Zn, and S) of different NPs by EDS.

Samples	N	O	Zn	S
ZIF	76.13	8.83	14.99	0.05
ZIF-SDSSD	76.81	8.16	14.89	0.14
ZIF-H_2S	77.48	7.79	14.63	0.11
ZIF-H_2S-SDSSD	75.50	9.71	14.59	0.20

Table S2. BET surfacr areas and Langmuir surface areas of different NPs.

	BET surface area	Langmuir surface area
ZIF	1444.2881	2242.1948
ZIF-SDSSD	1326.1803	2012.8812
ZIF-H_2S	1358.8831	2085.0341
ZIF-H_2S-SDSSD	1328.8104	1992.3241

Table S3. DLS examination of different NPs.

	Average particle size	Polymer dispersity index
ZIF	152.5±30.11	0.3577
ZIF-SDSSD	211.4±72.17	0.2674
ZIF-H_2S	158.2±33.6	0.3349
ZIF-H_2S-SDSSD	200±73.97	0.2084

Table S4. Primer sequences used in RT-qPCR.

	Forward	Reverse
Inos	GTTCTCAGCCCAACAATACAAGA	GTGGACGGGTCGATGTCAC
Il-1β	GCAACTGTTCCTGAACTCAACT	ATCTTTTGGGGTCCGTCAACT
Il-6	TAGTCCTTCCTACCCCAATTTCC	TTGGTCCTTAGCCACTCCTTC
Arg1	CTCCAAGCCAAAGTCCTTAGAG	AGGAGCTGTCATTAGGGACATC
Il-10	GCTCTTACTGACTGGCATGAG	CGCAGCTCTAGGAGCATGTG
Tgf-β	TCGACATGGATCAGTTTATGCG	CCCTGGTACTGTTGTAGATGGA
Runx2	GGGAACCAAGAAGGCACAGA	GGATGAGGAATGCGCCCTAA
Sp7	ATGGCGTCCTCTCTGCTTG	TGAAAGGTCAGCGTATGGCTT
Ocn	TTGGCCCAGACCTAGCAGAC	CTGGGCTTGGCATCTGTGAG
Opn	AGCAAGAAACTCTTCCAAGCAA	GTGAGATTCGTCAGATTCATCCG
Ctsk	GAAGAAGACTCACCAGAAGCAG	TCCAGGTTATGGGCAGAGATT
Mmp9	TCACCATGAGTCCCTGGCA	ATAGCGGTACAAGTATGCCTCTGC
Nfatc1	GACCCGGAGTTCGACTTCG	TGACACTAGGGGACACATAACTG
Atp6v0d2	CAGAGCTGTACTTCAATGTGGAC	AGGTCTCACACTGCACTAGGT